THE ELECTRONIC STRUCTURE OF Fe^{2+} IN REACTION CENTERS FROM *RHODOPSEUDOMONAS SPHAEROIDES*

III. EPR Measurements of the Reduced Acceptor Complex

W. F. BUTLER, R. CALVO, D. R. FREDKIN, R. A. ISAACSON, M. Y. OKAMURA, AND G. FEHER
Department of Physics, University of California, San Diego, La Jolla, California 92093

ABSTRACT Electron paramagnetic resonance (EPR) spectra of the reduced quinone-iron acceptor complex in reaction centers were measured in a variety of environments and compared with spectra calculated from a theoretical model. Spectra were obtained at microwave frequencies of 1, 9, and 35 GHz and at temperatures from 1.4 to 30 K. The spectra are characterized by a broad absorption peak centered at $g = 1.8$ with wings extending from $g \approx 5$ to $g < 0.8$. The peak is split with the low-field component increasing in amplitude with temperature. The theoretical model is based on a spin Hamiltonian, in which the reduced quinone, Q^-, interacts magnetically with Fe^{2+}. In this model the ground manifold of the interacting Q^-Fe^{2+} system has two lowest doublets that are separated by ~3 K. Both perturbation analyses and exact numerical calculations were used to show how the observed spectrum arises from these two doublets. The following spin Hamiltonian parameters optimized the agreement between simulated and observed spectra: the electronic g tensor $g_{Fe,x} = 2.16$, $g_{Fe,y} = 2.27$, $g_{Fez} = 2.04$, the crystal field parameters $D = 7.60$ K and $E/D = 0.25$, and the antiferromagnetic magnetic interaction tensor, $J_x = -0.13$ K, $J_y = -0.58$ K, $J_z = -0.58$ K. The model accounts well for the g value (1.8) of the broad peak, the observed splitting of the peak, the high and low g value wings, and the observed temperature dependence of the shape of the spectra. The structural implications of the value of the magnetic interaction, **J**, and the influence of the environment on the spin Hamiltonian parameters are discussed. The similarity of spectra and relaxation times observed from the primary and secondary acceptor complexes $Q_A^-Fe^{2+}$ and $Fe^{2+}Q_B^-$ leads to the conclusion that the Fe^{2+} is approximately equidistant from Q_A and Q_B.

INTRODUCTION

The reaction center (RC) is a bacteriochlorophyll-protein complex that catalyzes the primary photochemistry in bacterial photosynthesis (for recent reviews, see Okamura et al., 1982; Feher and Okamura, 1978). The trapping of the photon energy involves the oxidation of a primary donor and the concomitant reduction of a primary acceptor,[1] $DA \rightarrow D^+A^-$. The oxidized primary donor gives rise to a narrow EPR signal at $g = 2.0026$ first observed by Sogo et al., 1959. EPR and ENDOR (electron nuclear double resonance) studies of this signal have been instrumental in assigning the donor signal to a specialized bacteriochlorophyll dimer (Norris et al., 1973, 1975; Feher et al., 1973, 1975). The reduced primary acceptor gives rise to a broad EPR signal, centered at $g = 1.8$, which is observable at cryogenic temperatures (McElroy et al., 1970; Feher, 1971; Leigh and Dutton, 1972; Dutton et al.,1973). A similar broad EPR signal at $g = 1.8$ is observed when the secondary acceptor is reduced (Okamura et al., 1978; Wraight, 1978). An understanding of these EPR signals is necessary for the determination of the structure and electronic states of the acceptor species that play a vital role in the electron transfer reactions in photosynthesis. This paper presents experimental results and theoretical simulations of the EPR spectra, which elucidate the structure of the primary and secondary acceptors. In particular, we firmly establish the assignment of the acceptors as quinone-iron complexes (Q^-Fe^{2+}) and we determine the electronic structure of Fe^{2+} in these complexes and the magnetic interaction between Q^- and Fe^{2+}.

The assignment of the broad EPR signal to a quinone-iron complex is based on many indirect observations. Because broad EPR signals are frequently characteristic of transition metal ions, and since the RC was found to contain one Fe per RC, it was initially suggested that the signal might be due to a reduced state of Fe serving as the

---

Work performed by W. F. Butler in partial fulfillment of the requirements for the Ph.D. W. F. Butler's present address is Naval Ocean Systems Center (NOSC), San Diego, CA.

R. Calvo's present address is Instituto Venezolano de Investigaciones Cientificas (IVIC), Caracas Venezuela.

Reprint requests should be addressed to G. Feher.

[1]By primary acceptor we mean the first reduced species whose reoxidation rate is slow compared with its fluorescence lifetime (Cramer and Crofts, 1982), i.e., a species whose lifetime is >100 ns (Bolton, 1978).

primary acceptor (Feher, 1971). Subsequent experiments involving Fe removal (Loach and Hall, 1972) and replacement with Mn (Feher et al., 1974), however, have shown that Fe is not necessary for primary photochemical activity. Furthermore, Mossbauer (Debrunner et al., 1975; Boso et al., 1981a,b), magnetization (Butler et al., 1978, 1980), and EXAFS (Eisenberger et al. 1982; Bunker et al., 1982) measurements on Fe in RCs have shown that Fe exists as Fe^{2+} and does not change valence when the acceptor is reduced. On the other hand, a large number of experiments (e.g., EPR studies in Fe-free RCs [Loach and Hall, 1972; Feher et al., 1972], optical spectroscopy [Clayton and Straley, 1972; Slooten, 1972] and quinone removal and replacement [Cogdell et al., 1974; Okamura et al., 1975; Halsey and Parson, 1974]) have shown that both the primary and secondary acceptors are bound quinone molecules, Q_A and Q_B, respectively. To reconcile the broad EPR signal of the reduced acceptor in intact RCs with the identification of the acceptor as a quinone molecule, a quinone-Fe complex (ferroquinone) was proposed (Okamura et al., 1975). The electron in this complex is localized on the quinone, which is near an Fe^{2+}; the broad EPR signal results from a magnetic interaction between Q^- and Fe^{2+}.

How the broad EPR signal arises from this complex upon single electron reduction of either Q_A or Q_B has not been understood. In this paper we propose an answer to this question with a theoretical model of the ferroquinone complex based on the spin Hamiltonian formalism. In the first part of this study (Butler et al., 1980) we measured the magnetization of both unreduced and reduced RCs. From these measurements we obtained values of the spin Hamiltonian parameters D, E and the isotropic g value, which describe the electronic state of Fe^{2+}. In addition, we obtained an estimate of the magnitude of an isotropic exchange interaction J between Fe^{2+} and Q^-. In the second part of this study (Eisenberger et al., 1982), EXAFS measurements of RCs were used to determine the distances and numbers of the nearest neighbors of Fe^{2+}.

We have used these previously determined parameters as the starting point for our theoretical treatment of the $g = 1.8$ EPR spectrum. Refinement of these parameters, most notably the introduction of an anisotropic magnetic interaction, have allowed us to obtain a satisfactory agreement between observed and calculated EPR spectra. We present, in addition to a detailed numerical treatment of the theory, elementary and detailed perturbation treatments that develop physical intuition for the theory. An important feature of our theory is that the EPR spectrum arises from two closely spaced doublet levels; the theory correctly predicts the observed temperature dependence of the shape of the EPR spectrum.

The refined spin Hamiltonian parameters reflect the structure of the Q^-Fe^{2+} complex. In particular, the magnetic interaction is related to the Q^-Fe^{2+} distance and to the overlap of electronic wavefunctions. The origin of the values of the magnetic interaction are discussed in terms of the structure of the complex. A preliminary account of this work has been presented earlier (Butler et al., 1978).

MATERIALS AND METHODS

Sample Preparation

Chromatophores. Chromatophores were obtained from *Rhodopseudomonas sphaeroides* R-26 as described previously (Feher and Okamura, 1978). The chromatophore sample was prepared by suspending chromatophores, $A^{l\,cm}_{865} \simeq 100$, in 10 mM Tris-Cl, pH 8. This sample was reduced by adding anaerobically (to final concentrations) 50 mM sodium dithionite, 100 mM Tris-Cl, pH 8.

Reaction Centers. RCs were prepared in different detergents as follows:

(*a*) RCs were extracted from chromatophores and purified as previously described (Feher and Okamura, 1978). The detergent buffer solution was 0.025% LDAO, 10 mM Tris-Cl, pH 8 (TL buffer). RC samples with a "frozen in" narrow donor EPR signal, D^+ (see Fig. 1 *A*), were obtained by adding 5 mM ferricyanide to RCs, $A^{l\,cm}_{802} = 10$, in TL buffer + 50% glycerol and freezing the sample under illumination.

(*b*) RCs in 0.1% Triton X-100, 10 mM Tris-Cl, pH 8 (TT buffer) were obtained by adding 0.1% Triton X-100 to RCs, $A^{l\,cm}_{802} = 5$, in TL buffer and dialyzing for 2 d against TT buffer. RCs at high concentration in TT buffer ($A^{l\,cm}_{802} \sim 300$) were obtained by ultrafiltration as described in Butler et al., 1980. Reduced samples were obtained by adding sodium dithionite anaerobically to RCs in TT buffer as described (Butler et al., 1980). These samples contained 1.00 ± 0.05 quinone/RC. The secondary quinone was removed according to the procedure of Okamura et al. (1975).

(*c*) The LDAO in RCs in TL buffer was exchanged for sodium cholate by dialysis at 4°C for 1 d against 1% Na-cholate, 10 mM Tris-Cl, pH 8 buffer, followed by dialysis at 4°C for 3 d against 0.025% Na-cholate, 10 mM Tris-Cl, pH 8 buffer.

(*d*) Chromatophores, $A^{l\,cm}_{865} \simeq 100$, were suspended in 0.6% β-octyl-glucoside, 10 mM Tris-Cl, pH 8, and centrifuged at 200,000 *g* for 1 h. The pellet was suspended in 1.2% β-octyl-glucoside, 10 mM Tris-Cl, pH 8 and centrifuged at 250,000g for 1 h. RCs in the supernatant were purified by binding to a cytochrome *c* sepharose column (Brudvig et al., 1983) containing 2 μmol cyt *c*/ml. The amount of RC binding was ~ 20 μmol/ml. The RCs were eluted with a KCl gradient (0.05–0.25 M) containing 1% β-octyl-glucoside. The RCs were further purified by chromatography on DEAE cellulose in the presence of 1% β-octyl-glucoside and concentrated by ultrafiltration. The concentrated sample was dialyzed vs 1% β-octyl-glucoside, 10 mM Tris-Cl, pH 8. The ratio of optical absorbances $A^{l\,cm}_{280}/A^{l\,cm}_{802}$ was 1.25, which is close to the value (1.20) reported for the highest purity RC preparations (Feher and Okamura, 1978).

All RC preparations contained 0.94 ± 0.03 Fe/RC and < 0.03 heme/RC, both determined as described in Butler et al., 1980, and 1.8 ± 0.1 quinones/RC unless otherwise noted. The quinone content was determined by techniques described in Butler et al., 1980.

LM Subunit. The LM subunit was prepared from RCs in Na-cholate by precipitating the H subunit in 1 M $LiClO_4$ as previously described (Feher and Okamura, 1978). Na-cholate was used instead of LDAO to stabilize the LM subunit. The LM subunit contained 0.90 ± 0.05 Fe/LM and from 1 to 2 UQ/LM (see Debus, Okamura, and Feher, in preparation).

One-Flash, Two-Flash, and Three-Flash Samples. The samples used to study the EPR signals of the acceptor complex reduced with one, two, and three electrons contained 120 μM RCs and 1 mM

reduced cytochrome *c* in 0.025% LDAO, 10 mM Tris-Cl, pH 8. A 100 μml sample, in a 1 mm pathlength cuvette, was given 1, 2, or 3 laser flashes (Phase-R Co., New Durham, NH DL 2100C, $\lambda \approx 590$ nm, 150 mJ, 0.4 μs duration) spaced 1 s apart, then removed, by applying pressure, within ~2 s to a rexolite tube, 8 mm i.d., precooled to 77 K. 10 successive aliquots were flashed, frozen and combined to give a total sample volume of 1 ml.

EPR Techniques

Most experiments were performed at 9 GHz with a few at 1 GHz and 35 GHz. The 9 GHz spectrometer is a modified version of a superheterodyne system described earlier (Feher, 1957; McElroy, 1970; McElroy et al., 1974). A cavity frequency tuner was added by inserting a 2-mm o.d., fused-quartz rod through the broad face at the position of maximum electric field of a TE102 rectangular cavity. The rod was driven via a threaded drum by means of a nylon cord that exited at the top of the Dewar. The maximum insertion depth of 5 mm produced a frequency shift of 70 MHz. This was sufficient to compensate for the frequency shift of ~30 MHz that occurs between 4.2 and 1.4 K, due to the change in the dielectric constant of helium. The tuner was found to be particularly useful in the investigation of the temperature dependence of the integrated area of the EPR spectrum. When the frequency shifts were not compensated for, the signal amplitudes could vary by as much as 15%, presumably due to standing waves in the system. By keeping the frequency constant, the relative amplitudes could be determined with an accuracy of ~2%.

The modulation of the EPR signal was accomplished either by light or magnetic field modulation depending on whether the Q^-Fe^{2+} complex was created by illumination or by chemical reduction. Each technique has certain advantages and disadvantages. With light modulation, as well as with temperature modulation (Feher et al., 1969), the signal is proportional to χ''; hence, its amplitude is inversely proportional to the line width. With magnetic field modulation, one observes $d\chi''/dH$, which is inversely proportional to the square of the line width. Thus, for broad signals, light modulation seems to have an advantage. An additional advantage of light modulation is that it is insensitive to cavity backgrounds and other spurious signals arising from light-insensitive impurities. The main disadvantage of light modulation is that the sample has to be optically thin, which limits the number of observable centers. In addition, the low modulation frequency[2] (3.6 Hz in our case) used in this technique requires special design considerations to reduce the ubiquitous $1/f$ noise. A special low-noise cavity coupler was designed (Isaacson, 1976), and all structures were made as rigid as possible. Another potential drawback is a concomitant temperature modulation (Feher et al., 1969). To avoid this problem, a sample holder that permitted direct contact of the sample with the liquid helium bath was used. It consisted of a 1-mm-thick quartz frame to which a 10 × 20 × 0.1 mm quartz cover slip was attached with silicon grease. Typically 0.1–0.2 ml of sample was poured into the frame and frozen prior to insertion into the precooled cavity. The light modulation was performed with an actinic light source and square-wave chopper as described previously (McElroy et al., 1974). To reduce the energy input to the cavity, a band-pass filter ($\lambda_0 = 850$ nm, $\Delta\lambda = 50$ nm [C850, Corion Corp., Holliston, MA]) was used.

When magnetic-field modulation was used, the sample holders were made from quartz or rexolite tubes with an inner diameter of 8 mm. Typically the sample volume was 1.3 ml. The modulation frequency was either 80 Hz when metal cavities were used or 100 kHz when silver-coated plastic or quartz cavities were used. The main problems encountered with field modulation were cavity background signals and baseline drifts. The background signal appeared to be due principally to Cu^{2+} contamination of the cavity wall and was subtracted from the spectra presented. The small baseline drift was usually of no consequence, except when the traces were integrated to obtain χ''. The integrated spectra were adjusted to give the same amplitude at 8 kG as observed with light modulation (see Fig. 1).

The 1-GHz spectrometer used a half-wavelength coaxial (TEM mode) cavity (Feher and Kip, 1955) followed by a circulator and low-noise preamplifier (Western Electric Co., New York, NY, model GF40105, 8.5 dB noise figure). The 35 GHz spectrometer was a modified Varian V4500 unit (Varian Associates Instrument Group, Palo Alto, CA). Both spec-

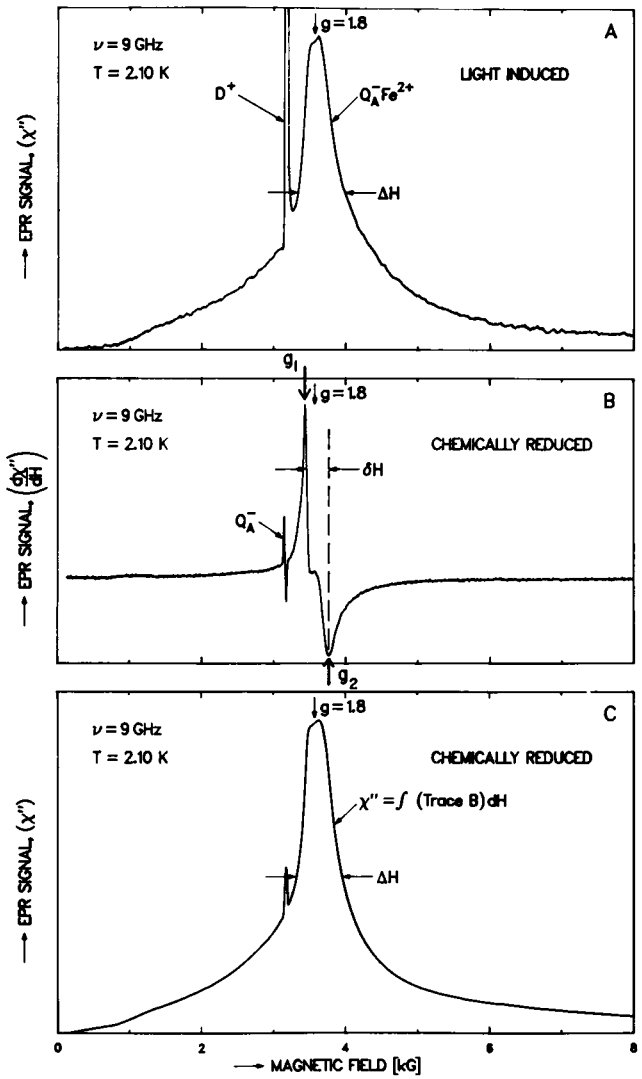

FIGURE 1 EPR spectra of RCs at low temperature. (*A*) Light-induced signal is proportional to χ''. It is composed of a narrow signal due to D^+ and a broad signal due to $Q_A^-Fe^{2+}$. (*B*) Chemically reduced RCs. The EPR signal, observed by field modulation, is proportional to $d\chi''/dH$. (*C*) Integral of the field modulation spectra. It is essentially the same as the light-induced spectrum, *A*. The small peak at $g = 2.0045$ is due to Q_A^- in reduced RCs with no Fe^{2+}. Spectra were normalized to arbitrary intensities. Sample used in *A*: RCs, $A_{802}^{1\,cm} = 150$ with 1 UQ/RC, in 0.1% Triton X-100, 10 mM Tris-Cl, pH = 8 (TT buffer), and 50% glycerol, frozen in the dark in a flat quartz cell 8 mm × 18 mm × 1 mm. Sample used in *B* and *C*: RCs, $A_{802}^{1\,cm} = 285$ with 1 UQ/RC, in TT buffer, reduced with 100 μml of 1 M sodium dithionite in 1 M Tris-Cl pH 8, in an 8 mm i.d. rexolite tube.

[2]The modulation frequency has to be low in comparison with the recombination kinetics of the charge separated species $D^+ A^-$ (McElroy, et al., 1974).

trometers used the same Dewar and lock-in detection system as the 9 GHz spectrometer.

Magnetic field sweeps were controlled in all three spectrometers by Varian Fieldials and calibrated with a Varian F-8 NMR Fluxmeter (Varian Associates). A Nicolet 1180 minicomputer (Nicolet Instrument Corp., Madison, WI) was used for signal averaging and data processing. Cryogenic temperatures were obtained with a conventional double-Dewar system, the cavity with sample being immersed in liquid helium. In the 9 and 35 GHz spectrometers, the samples could be inserted and removed from the cavity while it remained at low temperature. To eliminate noise produced by bubbles in the cryogenic liquids, the nitrogen as well as helium above the λ point (2.17 K) were supercooled by periodic gentle pumping. Temperatures below 4.2 K were measured with a pressure gauge (Wallace & Tiernan Div., Pennwalt Corp., Belleville, NJ) and above 4.2 K with a calibrated carbon resistor.

Computational Techniques

The numerical techniques to calculate the EPR spectrum from the spin Hamiltonian are described in the theory section and Appendix B. We implemented these calculations in a system of FORTRAN programs using a VAX 11/780 computer (Digital Equipment Corp., Maynard, MA). Several commercially available software packages were used: EISPACK (Argonne National Laboratory, see Smith et al., 1976) for solving eigenvalue problems; IMSL (IMSL, Inc., Houston, TX) for mathematics utility programs; spline computation subroutines of de Boor (1978) (available from IMSL); and the DISSPLA plotting package (ISSCO, Inc., San Diego, CA).

EXPERIMENTAL RESULTS

The reaction center has two quinone binding sites to which the primary and secondary electron acceptors, designated Q_A and Q_B, are attached. Several paramagnetic species can be formed depending on the reduction states of the two quinones (Okamura et al., 1978; Wraight, 1978; Rutherford and Evans, 1980). For simplicity, we started with RCs from which Q_B had been removed (Okamura et al., 1975); the paramagnetic species that we are, therefore, concerned with here is $Q_A^-Fe^{2+}$. In the next few sections we shall deal in detail with the EPR spectrum of this complex and in later sections with the other paramagnetic species (e.g., $Fe^{2+}Q_B^-$).

Comparison of the Light-induced EPR Spectrum of the $Q_A^-Fe^{2+}$ Complex with That Obtained by Chemical Reduction

The $Q_A^-Fe^{2+}$ complex (in association with either D^+ or D) can be formed either by illuminating the RC sample at cryogenic temperatures (McElroy et al., 1970; Feher, 1971) or by chemically reducing the sample (e.g., with sodium dithionite) at room temperature and subsequently lowering its temperature (Leigh and Dutton, 1972; Dutton et al., 1973). These two procedures can be described by

$$DQ_AFe^{2+} \xrightarrow{h\nu} D^+Q_A^-Fe^{2+} \quad (1)$$

$$DQ_AFe^{2+} \xrightarrow{Na_2S_2O_4} DQ_A^-Fe^{2+} \quad (2)$$

where D is a bacteriochlorophyll dimer that serves as the primary donor in the charge separation process.

The low-temperature EPR spectra obtained from the $Q_A^-Fe^{2+}$ complex produced by these two methods are shown in Fig. 1. The light-induced absorption signal (Fig. 1 *A*) is proportional to the susceptibility χ''. It was composed of a large, narrow signal at $g = 2.0026$ due to D^+ (McElroy et al., 1972) and a broad signal at $g = 1.8$[3] (Feher, 1971) due to $Q_A^-Fe^{2+}$. Its line width, ΔH (full width at half maximum), at 9.0 GHz was 640 ± 30 G (Gauss). Because the areas under the two peaks were approximately the same (for a more complete discussion, see subsequent section on integrated area), the amplitude of the narrow signal was larger than that of the broad signal by the ratio of their line widths $[\Delta H(g = 1.8)/\Delta H(g = 2.0026) \simeq 50]$.

The EPR signal of the chemically reduced sample was proportional to the derivative $d\chi''/dH$ (Fig. 1 *B*), which is a consequence of the magnetic-field modulation used. Its line width δH (full width between extrema) was 330 ± 15 G. The positions of the extrema can be characterized by two effective g values g_1 and g_2 (see Fig. 1 *B*), that were found to be 1.840 and 1.681, respectively (see Table I).

By integrating the trace of Fig. 1 *B*, one obtains the trace shown in Fig. 1 *C*. It is essentially the same as in Fig. 1 *A*, except for the absence of the D^+ peak (see Eq. 2). The small, narrow peak that occured at $g = 2.0045$ was due to reduced quinone, Q_A^-, in RCs that have lost the Fe^{2+}. Their percentage was estimated from the area under the Q_A^- peak to be ~ 1%. Because field and light modulation produce basically the same broad $g = 1.8$ signal, these two techniques have been used interchangeably throughout this work.

Effect of the Environment on the EPR Parameters

The line widths at 2.1 K and 9 GHz, shown in Fig. 1, are typical of RCs at a protein concentration ≥30 mg/ml ($A_{802}^{1\,cm} \approx 100$). The line widths observed in different RC samples that were nominally prepared under the same conditions varied by 10–15%. This was in excess of the precision with which the line widths were measured (~5%) and was presumably due to the sensitivity of the line width to the exact conformational state of the RC. In an attempt to understand the origin of these variations, we changed several external parameters that were thought to affect the environment of the iron.

The line width alone does not, of course, provide a complete description of the line shape. A more adequate description, for instance, would be a tabulation of the moments of the line (see, e.g., Poole, 1983). We did not feel that the present work warranted such a detailed description. Instead, we used the ratio of the line widths of χ'' and

[3]Because the peak of the broad line shows some structure, it does not make sense to quote g values with a higher precision to describe χ''. However, in the case of $d\chi''/dH$, the two extrema can be determined with higher precision; they are operationally characterized by g_1 and g_2 (see Fig. 1 *B*).

TABLE I

EPR PARAMETERS OF THE $Q_A^-Fe^{2+}$ COMPLEX IN REACTION CENTERS FROM *R. SPHAEROIDES* R-26

T = 2.1 K ν = 9.0 GHz

No.	Sample	ΔH^* (χ'') ± 5%	$\delta H\ddagger\left(\frac{d\chi''}{dH}\right)$ ± 5%	$\frac{\Delta H}{\delta H}$	g_1§ ± 0.001	g_2§ ± 0.002
1	RC in TT buffer‖	640	330	1.88	1.840	1.681
2	RC + *o*-phen (TT buffer)¶	360	230	1.56	1.839	1.726
3	*RC in TL buffer***	*610*	*270*	*2.26*	*1.840*	*1.708*
4	*RC* + *o*-phen (TL buffer)***	370	260	1.42	1.837	1.710
5	RC in Na-cholate‡‡	580	250	2.32	1.839	1.716
6	RC in Na-cholate + *o*-phen***	390	230	1.68	1.839	1.726
7	RC in β-o-glucoside§§	560	240	2.33	1.840	1.722
8	RC in β-o-gluc. + *o*-phen***	405	250	1.62	1.837	1.715
9	Chromatophores‖‖	440	260	1.69	1.839	1.712
10	Chrom. + *o*-phen***	380	230	1.65	1.839	1.726
11	LM-subunit¶¶	480	265	1.81	1.841	1.711
12	LM + *o*-phen***	475	255	1.86	1.838	1.713

*ΔH—full width at half maximum of χ'' (see Fig. 1A)

‡δH—full width between extrema of $d\chi''/dH$ (see Fig. 1B)

§*g*-values refer to the extrema of the derivative spectrum

‖Sample described in the caption of Fig. 1

¶Sample described in the caption of Fig. 2

**$A_{802}^{1\,cm}$ = 10, 0.025% LDAO, 10 mM Tris-Cl pH 8, 50% glycerol

‡‡$A_{802}^{1\,cm}$ = 10, 0.025% Na-cholate, 10 mM Tris-Cl pH 8, 50% glycerol

§§$A_{802}^{1\,cm}$ = 10, 1% β-o-glucoside, 10 mM Tris-Cl pH 8, 50% glycerol

‖‖$A_{865}^{1\,cm}$ = 100, 50 mM dithionite, 100 mM tris-Cl pH 8

¶¶$A_{802}^{1\,cm}$ = 10, 0.025% Na-cholate, 10 mM tris-Cl pH 8, 50% glycerol

***Same as preceding sample + 10 mM *o*-phenanthroline

Samples 1 and 2 were in rexolite tubes (8 mm i.d.), the rest were in flat quartz cells (8 mm × 18 mm × 1 mm).

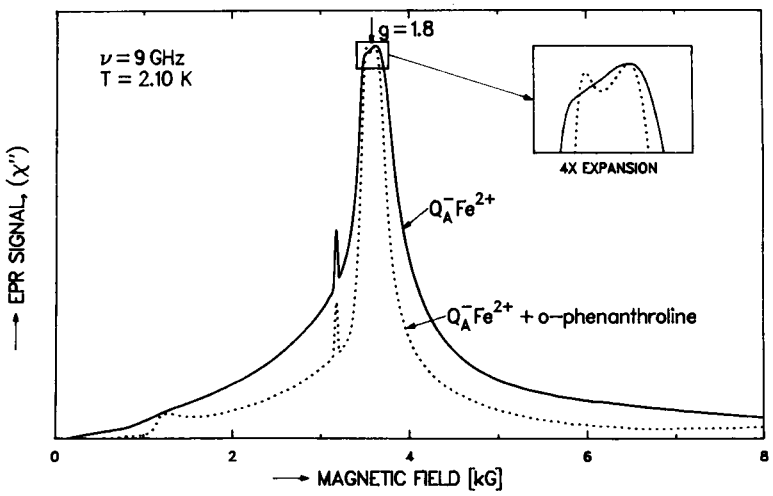

FIGURE 2 Comparison of EPR spectra of RCs with and without *o*-phenanthroline. The *o*-phenanthroline sample shows significant narrowing; the concomitant increase in resolution reveals a split peak and a pronounced low-field edge at ~1.2 kG. The RC sample was the same used to obtain Fig. 1 *B*. 10 mM *o*-phenanthroline was added to a similar sample to obtain the narrowed spectrum (dotted). Both spectra were obtained by integrating field modulation spectra (see Fig. 1 *C*).

$d\chi''/dH$ as an empirical index of the line shape.[4] The observed ratios are tabulated in Table I together with the effective g values (g_1 and g_2) corresponding to the extrema of the $d\chi''/dH$ spectra.

Effect of o-Phenanthroline. *o*-phenanthroline inhibits electron transfer from Q_A to Q_B (Parson and Case, 1970; Clayton et al., 1972) and is believed to bind to the reaction center in the vicinity of the Fe^{2+}. Its presence has a dramatic effect on the line shape as shown in Fig. 2. The line width ΔH was reduced from ~640 to 360 G and δH from 330 to 230 G (see Table I). In addition, two new features appeared in the spectrum: the peak at $g = 1.8$ is split (see inset in Fig. 2) and an absorption edge appears at $H \approx 1.2$ kG. The emergence of these features was presumably a consequence of the narrowing of the line that produced enhanced resolution. The assignment of the low-field edge was a source of some concern, since it appeared close to $g = 6$, where high-spin Fe^{3+} (e.g., in oxidized cytochrome *b*) often exhibits a resonance. However, the fact that RCs without *o*-phenanthroline exhibited a smaller and much broader edge (barely discernible in Fig. 2) argues against a contamination.[5] In addition, the temperature dependence of the amplitude of the edge absorption, together with theoretical expectations, provides evidence that the edge is associated with the $Q_A^-Fe^{2+}$ complex (see Detailed Comparison section on the low-field edge).

Effect of Freezing. In the early 9 GHz experiments (McElroy et al., 1970; Feher, 1971), additional smaller peaks were observed at 0.7, 1.7, and 2.7 kG. The lines at 0.7 and 1.7 kG were assigned to Mn^{2+} substituting for Fe^{2+} in some RCs (Feher et al., 1974). However the line at 2.7 kG was observed even in Mn-free RCs and was assigned to $Q_A^-Fe^{2+}$ complexes in which Fe^{2+} was in a different environment. The 2.7 kG peak could be eliminated by freezing the sample in 50% glycerol or 25% sucrose. Under these conditions the crystallization of water is inhibited. We believe, therefore, that the 2.7 kG peak was brought about by disruption of the native protein by ice crystallites. The 2.7 kG peak also disappeared at high RC concentrations ($A_{802}^{1\,cm} > 20$). Under these conditions, crystallization is presumably also inhibited, or, alternatively, aggregation of RCs during freezing may exert a protective effect. The most conclusive evidence that the 2.7 kG peak is not associated with native RCs comes from the EPR spectra of chromatophores. They do not show the 2.7 kG peak.

Effect of Detergents. The LDAO used in preparing the RCs was exchanged on a column or dialyzed against cholate and Triton (see Materials and Methods). Since it is known that LDAO cannot be completely removed (Feher and Okamura, 1978), RCs were also prepared without LDAO using the mildest known effective detergent, β-octyl-glucoside. In this purification procedure, a cytochrome *c* affinity chromatography column was used, thereby obviating the use of ammonium sulfate, a potentially harmful step.

The results are shown in Table I. The line width, ΔH, in the absence of *o*-phenanthroline varied between 560 and 640 G; *o*-phenanthroline had a marked narrowing effect in all cases. The width, δH, was less affected by *o*-phenanthroline, the largest effect being observed for the high-

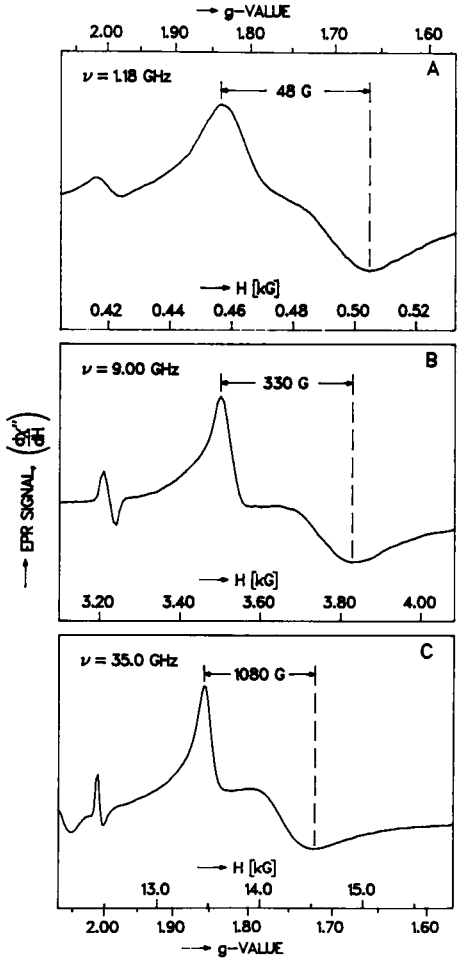

FIGURE 3 Field modulation spectra of RCs at 1.18, 9.00, and 35.0 GHz. The line width δH is approximately proportional to frequency; the peak of the spectrum ($d\chi''/dH = 0$) occurs at $\sim g = 1.8$ for all frequencies. The sample at 1.18 and 9.00 GHz was the same as that for Fig. 1 *B*. The sample used at 35 GHz was similar except $A_{802}^{1\,cm} = 325$ and a 2-mm i.d. quartz tube was used.

[4]For a Gaussian line shape this ratio is 1.18 and for a Lorentzian 1.73. There is no theoretical reason why either of these cases should apply to the EPR lines discussed in this paper.

[5]If *o*-phenanthroline were to remove and chelate Fe^{2+} from the RC, it would be expected to form a low-spin (diamagnetic) Tris complex (Cotton and Wilkinson, 1972) that would not give rise to a $g = 6$ signal.

concentration Triton sample (No. 1). The g values of the low-field peak remained constant for all samples (g_1 = 1.839 ± 0.001), whereas g_2 varied in accordance with the different line widths.

RCs in Chromatophores. To determine to what extent the extraction and purification of RCs affects the EPR spectrum, the line shapes of RCs in their native states, i.e., in chromatophores, were investigated. The results showed that the widths, ΔH, of purified RCs were larger than those observed in chromatophores (see Table I). However, in the presence of *o*-phenanthroline, the narrowed spectral widths were similar in RCs and chromatophores, suggesting that bound *o*-phenanthroline tends to restore the native conformation of RCs in the vicinity of the quinone-iron complex.

Effect of Removal of the H Subunit. It has been shown that when one of the subunits (H) is removed from the RC, the remaining two subunits (LM) are capable of producing the primary charge separation (Feher and Okamura, 1978; Debus et al., 1981, Debus, Okamura, and Feher, in preparation). The line width ΔH observed in these LM complexes was significantly narrower than in RCs without *o*-phenanthroline (see Table I). Another interesting feature was that the addition of *o*-phenanthroline to the LM complex did not produce a significant narrowing of the line width. This suggests that the removal

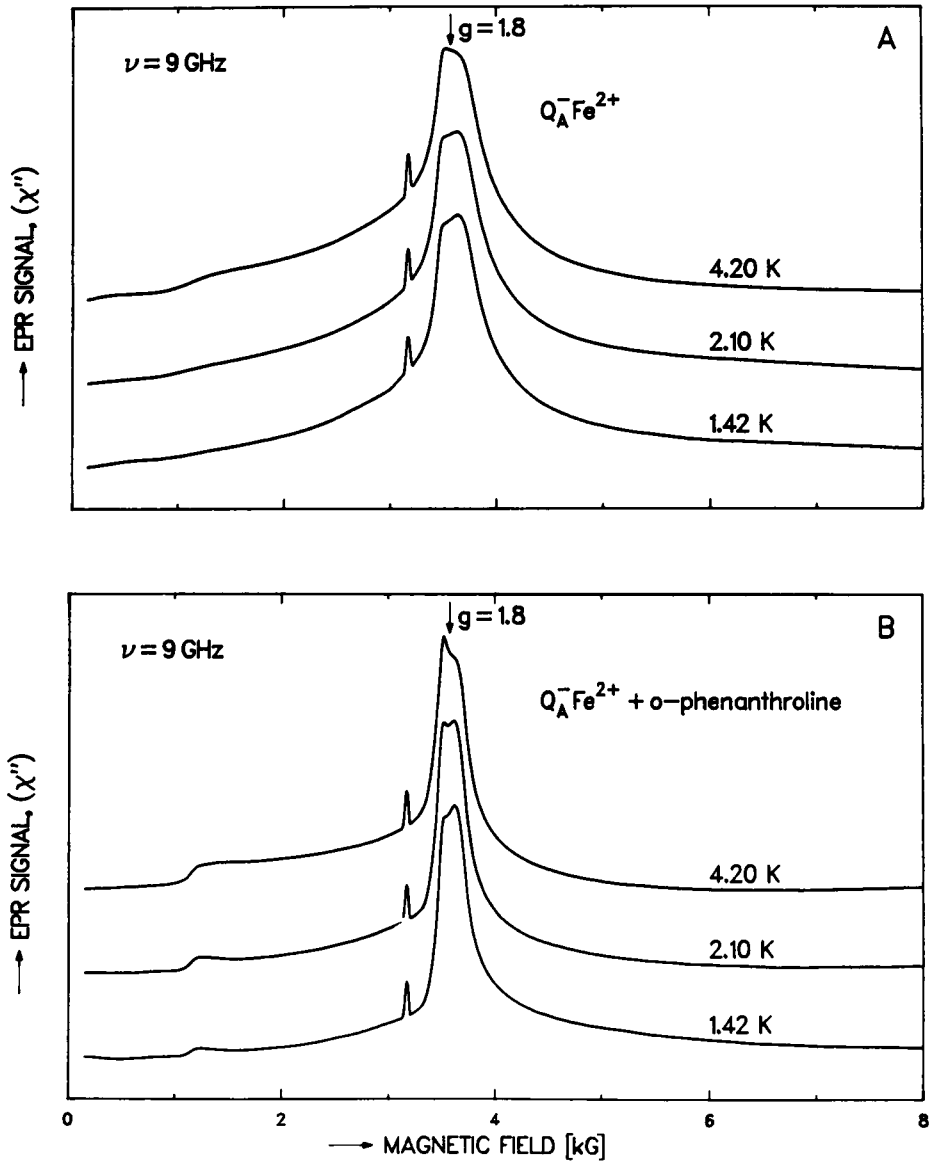

FIGURE 4 Temperature dependence of EPR spectra of RCs (*A*) and RCs + *o*-phenanthroline (*B*) at low temperatures. The relative intensities of the low- and high-field sides of the peak, as well as the low-field edge in *B*, are temperature dependent, whereas the peak positions and line widths are not. The small narrow peaks at 3.2 kG are from Q_A^- in RCs that lost their Fe^{2+}. The RC sample is the same as described in the legend of Fig. 1 *B*; the RC + *o*-phenanthroline sample is the same as described in the legend of Fig. 2.

of H results in the loss of the *o*-phenanthroline binding site.

Effect of Quinones. In previous experiments, we replaced the native ubiquinone-50 with different quinones at the Q_A site and measured the line width ΔH (Okamura et al., 1975). ΔH of all ferroquinone complexes fell between 600 and 1,000 G. We also found that varying the occupancy of the Q_B site, before reduction and/or freezing of the sample, did not change the line width of $Q_A^-Fe^{2+}$, i.e., RCs with one and two quinones had similar line widths (detailed data not shown, although note that $Q_A^-Fe^{2+}Q_B^-$, Fig. 6 *C*, has the same line width δH as Q^-Fe^{2+}, Fig. 1 *B*).

Frequency Dependence of the Spectrum

To understand the origin of the line width and to check whether the concept of a *g* value is applicable, EPR spectra were taken at three frequencies: 1.18, 9.00, and 35.0 GHz. The results (Fig. 3) showed that (*a*) the line width was approximately proportional to the applied frequency, i.e., $\delta H/H_0 \simeq$ constant; (*b*) the peak of the line (i.e., the field H_0 where $d\chi''/dH$ crosses zero) occured at approximately the same $g = 1.8$ value; and (*c*) the higher the frequency the more structure was resolved in the region of $g = 1.8$ (at 35 GHz the slope changes sign around $g = 1.8$).

Microwave Saturation Behavior of the EPR Line

In taking the spectra discussed in the previous sections, care was taken to reduce the microwave power below a level at which saturation effects occurred. The spin-lattice relaxation time of the $Q_A^-Fe^{2+}$ complex has been studied in detail by pulse techniques (Calvo et al., 1982) and will be the topic of a separate publication (Calvo, Butler, Isaacson, Okamura, Fredkin, and Feher, in preparation). The relaxation rate was found to depend exponentially on temperature and to be governed by transitions between the Fe levels. In this work, the saturation behavior of the EPR signal was obtained by measuring χ'' vs. microwave power. At 2.1 K, χ'' was reduced to half its unsaturated value at a microwave power of 13 mW for the RC sample No. 1 (Table I), and 9 mW for the RC + *o*-phenanthroline sample No. 2. (The microwave cavity was matched to the waveguide and had a loaded Q of 8,000). The functional dependence of χ'' on microwave power corresponded to an inhomogeneously broadened line (Portis, 1953), i.e., χ'' was proportional to $(1 + CP)^{-1/2}$ where P is the microwave power and C a proportionality constant that is proportional to the spin-lattice relaxation time T_1.

Temperature Dependence of the Spectrum

Two types of changes in the EPR spectrum were observed with temperature. Below 4 K, the gross features (e.g., the line width) did not change. However, the finer structural details, i.e., the amplitudes of the split components of the line and the low-field edge varied with temperature (Fig. 4). These features were best seen in samples of RCs to which *o*-phenanthroline had been added (Fig. 4 *B*), although remnants of their presence could also be discerned in RC samples without *o*-phenanthroline (see Fig. 4 *A*). Above 4 K the line was starting to broaden and by 20 K the increased width was clearly discernible (see Fig. 5). Above 30 K the line became difficult to observe. In these high-temperature spectra there was no evidence of additional lines, which might have been expected on theoretical grounds (see Summary and Discussion).

Temperature Dependence of the Integrated Area of the EPR Spectra

Spectra similar to those of Fig. 1*A* were obtained by light modulation at temperatures of 1.4 and 4.2 K. The microwave cavity was tuned to insure that its resonant frequency was the same at both temperatures. To avoid temperature modulation (Feher et al., 1969) of the sample, flat cells (8 mm × 18 mm × 1 mm) were used, and their cover slides were removed to bring the RC sample into direct contact with the liquid helium. The RCs were in TL buffer at a concentration of $A_{802}^{1\,cm} = 10$. The spectra were integrated from 0 to 8 kG, either graphically or by a computer, and the contribution of the narrow signal due to D^+ was subtracted. The ratio of the integrated spectra was found to be

$$\text{for } Q_A^-Fe^{2+}: \quad \frac{\int_0^{8\,kG} \chi''dH \text{ at } 1.40\text{ K}}{\int_0^{8\,kG} \chi''dH \text{ at } 4.22\text{ K}} = 2.3 \pm 0.1. \tag{3}$$

As a control the integrated area of D^+ was obtained on a sample in which the narrow signal was "frozen in" by illuminating the RCs at room temperature in the presence of ferricyanide (see Materials and Methods). We found

$$\text{for } D^+: \quad \frac{\int_0^{8\,kG} \chi''dH \text{ at } 1.40\text{ K}}{\int_0^{8\,kG} \chi''dH \text{ at } 4.22\text{ K}} = 2.9 \pm 0.1. \tag{4}$$

For this case one expects the integrated area to be propor-

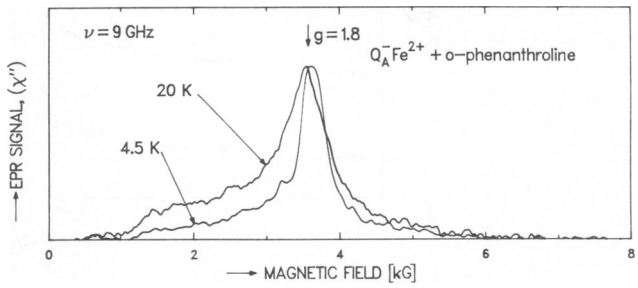

FIGURE 5 Light-modulated EPR spectra of RCs at 4 and 20 K. Sample was same as described in the legend of Fig. 2.

tional to $1/T$ (Curie law),[6] i.e., the ratio should be 4.22/1.40 = 3.0. The experimentally determined ratio for D^+ was in agreement with this value. No change in the amplitude of this signal was observed at either temperature when the sample was illuminated. This shows that negligible temperature modulation of the sample occurred.

Ratio of the Integrated Areas of the D^+ and $Q_A^-Fe^{2+}$ Spectra

In the previous section, we determined the temperature dependence of the integrated spectra of $Q_A^-Fe^{2+}$. The same sample was used to compare the integrated area of the $Q_A^-Fe^{2+}$ spectrum with that obtained from D^+ using light modulation. The following ratios were obtained at 4.22 K and 1.40 K:

$$\frac{\int_0^{8\,kG} \chi''(Q_A^-Fe^{2+})dH}{\int_0^{8\,kG} \chi''(D^+)dH} = \begin{cases} 2.2 \pm 0.1 \text{ at } 4.22\text{ K} \\ 2.8 \pm 0.1 \text{ at } 1.40\text{ K}. \end{cases} \quad (5)$$

To make a meaningful comparison with theory, the integrated spectrum of D^+ needs to be corrected. The reason is that the spin-lattice relaxation time, T_1, of D^+ is longer than its lifetime (i.e., the charge recombination time $D^+Q_A^- \rightarrow DQ_A$). Consequently, the magnetization of D^+ cannot build up to its maximum value (McElroy et al., 1974). We attempted to correct for this effect by measuring the amplitude of D^+ at 77 K where T_1 was very short and extrapolating the amplitude to 4.2 K using the known $1/T$ (Curie) dependence. Care was taken to correct for changes in the Q of the cavity with temperature. When this extrapolation was made, the ratio (Eq. 5) was found to be approximately unity at 4.22 K. However, the accuracy of this procedure was not sufficiently good (20–30%) to provide a critical test of the theory.

EPR Spectrum of the $Fe^{2+}Q_B^-$ Complex

Up to now we have discussed only the spectrum of $Q_A^-Fe^{2+}$. The $Fe^{2+}Q_B^-$ species can be trapped by illuminating the sample with a short laser flash in the presence of cytochrome *c*, which reduces D^+ and thereby prevents the recombination of the electron on Q_B^-. To test whether the electron transferred to Q_B^-, we also trapped the products after 2 and 3 laser flashes. The electron transfer after successive flashes is expected to proceed as follows (Vermeglio, 1977; Wraight, 1977; Okamura et al., 1978):

first flash $$DQ_AFe^{2+}Q_B \xrightarrow{h\nu} D^+Q_A^-Fe^{2+}Q_B$$

$$\xrightarrow[\text{cyt}-c]{\text{red}\quad\text{ox}} DQ_AFe^{2+}Q_B^- \quad (6)$$

second flash $$DQ_AFe^{2+}Q_B^- \xrightarrow{h\nu} D^+Q_A^-Fe^{2+}Q_B^-$$

$$\xrightarrow[\text{cyt}-c]{\text{red}\quad\text{ox}} DQ_AFe^{2+}Q_B^= \quad (7)$$

third flash $$DQ_AFe^{2+}Q_B^= \xrightarrow{h\nu} D^+Q_A^-Fe^{2+}Q_B^=$$

$$\xrightarrow[\text{cyt}-c]{\text{red}\quad\text{ox}} DQ_A^-Fe^{2+}Q_B^=. \quad (8)$$

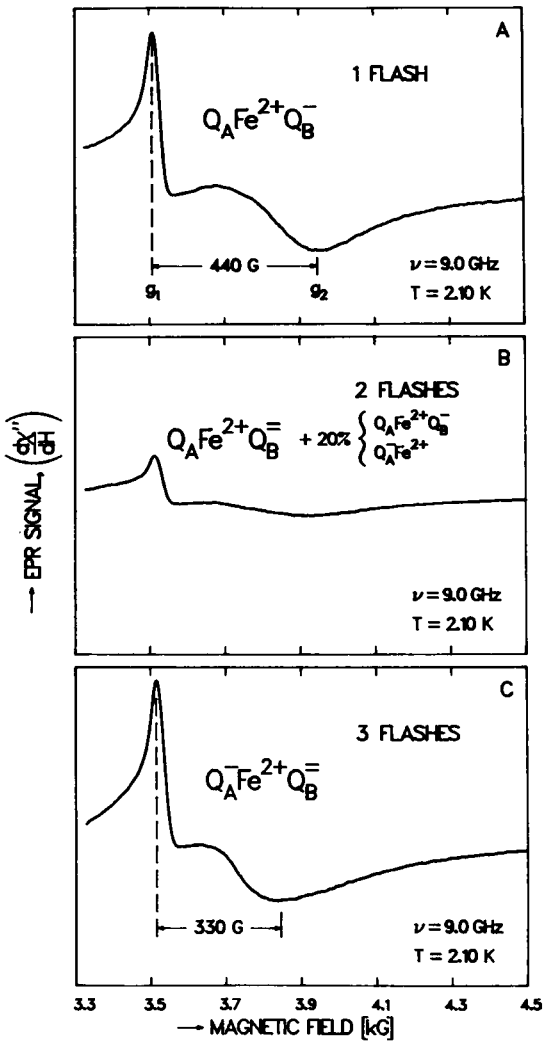

FIGURE 6 EPR spectra of RCs exposed to 1, 2, and 3 laser flashes. The spectra of the different charged species of $Q_AFe^{2+}Q_B$ subsequently formed are shown in *A*, *B*, and *C*. The line width δH of $Q_AFe^{2+}Q_B^-$ is ~100 G greater than for $Q_A^-Fe^{2+}Q_B^-$. The residual signal observed in *B* for $Q_A^-Fe^{2+}Q_B^-$ (which is diamagnetic) is explained in the text. The change in line width is almost entirely due to a shift in the high-field minimum of the spectrum. The samples (RCs, $A_{802}^{1\,cm}$ = 53, 2 UQ/RC, in TL buffer, 1 mM reduced cytochrome *c*) were illuminated with laser flashes at room temperature in a cuvette with a 1-mm path length, (8 mm × 20 mm) and removed by pressure (through a tube attached to the cuvette) within ~2 s after the flash into a precooled (T = 77 K) rexolite tube (8 mm i.d.).

[6]The exact expression for the magnetization (i.e., integrated area) is $M \propto \tanh[(g\mu_B H)/(2k_B T)]$. The simplified $1/T$ expression produced a maximum error of 0.07% at 1.4 K ($H \approx 3$ kG).

The experimental spectra of the products trapped at low temperatures are shown in Fig. 6. The position and general shape of the spectra due to $Q_A Fe^{2+} Q_B^-$ and $Q_A^- Fe^{2+} Q_B$ are similar. The main difference is the larger line width of $Q_A Fe^{2+} Q_B^-$. The EPR parameters for the two species are

$$\delta H = 440 \text{ G}; g_1 = 1.838, g_2 = 1.633 \quad \text{for } Q_A Fe^{2+} Q_B^-, \tag{9}$$

$$\delta H = 330 \text{ G}; g_1 = 1.841, g_2 = 1.681 \quad \text{for } Q_A^- Fe^{2+} Q_B. \tag{10}$$

The larger shift of g_2 with respect to g_1 was similar to the effect found in the different RC preparations (see Table I). We also measured the microwave saturation of the two species (refer to previous section on microwave saturation) and found that, at 2.1 K, $Q_A Fe^{2+} Q_B^-$ saturated at a microwave power that was 40% higher than that required for $Q_A^- Fe^{2+} Q_B$. This indicates that the spin-lattice relaxation time of $Fe^{2+} Q_B^-$ was ~40% shorter than that of $Q_A^- Fe^{2+}$. These results, with an appropriate model, should provide information on the relative distances of Q_A and Q_B to Fe^{2+} (see Summary and Discussion).

In the idealized scheme described by Eqs. 6–8, one would not expect a signal after two flashes since $DQ_A Fe^{2+} Q_B$ is not paramagnetic. However, a small signal was observed (Fig. 6 *B*). It is attributed to several effects that produce corrections to Eqs. 6–8: (*a*) a fraction of RCs (10–15%) had only one quinone and, therefore, gave rise to a $Q_A^- Fe^{2+}$ signal after 2 flashes; (*b*) due to the equilibrium between $Q_A^- Q_B$ and $Q_A Q_B^-$, ~6% of the population was in the $Q_A^- Q_B$ state (T = 23°C, pH = 8) (Kleinfeld, Okamura, and Feher, in preparation); (*c*) if the cytochrome reduction was not 100% effective or if the light flash did not saturate the entire sample, some $Fe^{2+} Q_B^-$ would have accumulated after the second flash. Thus, notwithstanding the small signal seen in Fig. 6 *B*, the main features predicted by Eqs. 6–8 are borne out by these experiments.

In addition to the two species discussed above, there is a third species, $D^+ Q_A^- Fe^{2+} Q_B^-$. It was obtained by illuminating at cryogenic temperatures the sample that had received one laser flash at room temperature (see Eq. 6). The resulting EPR signal exhibited a reduced amplitude of the g = 1.8 peak and an increase in the absorption of the high-field tail. This shows that Q_A and Q_B interact magnetically. A similar conclusion was reached by Wraight (1978).

Summary of the Main Features of the $Q_A^- Fe^{2+}$ Spectrum

Before proceeding to the theoretical treatment, we summarize here the main features of the $Q_A^- Fe^{2+}$ spectrum that need to be accounted for by theory.

(*a*) The EPR line (χ'') is an asymmetric line that is inhomogeneously broadened and several hundred Gauss wide, with a peak at $g \approx 1.8$ (see Fig. 1).

(*b*) The line width is approximately proportional to the microwave frequency (i.e., the external DC magnetic field); the g value of the χ'' peak is ~1.8, independent of the microwave frequency (see Fig. 3).

(*c*) The peak is split; the amplitude of the low-field component increases with temperature (see Fig. 4).

(*d*) A low-field absorption edge is observed at ~1 kG (ν = 9 GHz). Its amplitude increases with temperature (see Fig. 4).

(*e*) The temperature dependence of the integrated area of the EPR spectrum does not obey Curie's law.

(*f*) Variations in line width are observed in different samples (see Table I). The high-field extremum, g_2, of the derivative spectrum ($d\chi''/dH$) shifts significantly more than the low-field extremum, g_1.

(*g*) The qualitative features of the spectra of $Q_A^- Fe^{2+}$ and $Fe^{2+} Q_B^-$ are similar (see Fig. 6), although they differ in detail (Eqs. 9 and 10).

THEORY

We wish to model the electronic structure of Fe^{2+} and its interaction with Q^-. In Butler et al., 1980, we showed that a spin Hamiltonian (Butler et al., 1980, Eq. 3) could describe the magnetization of $Q^- Fe^{2+}$ in reduced RCs. That spin Hamiltonian had crystal field terms for the high spin, $S_{Fe} = 2$, Fe^{2+} ion, an isotropic g factor in the Zeeman term for Fe^{2+}, a Zeeman term for the $S_Q = 1/2$ Q^- ion and an iron-quinone magnetic interaction[7] with coupling constant J, which was assumed, for simplicity, to be isotropic. We found it necessary to generalize that Hamiltonian, replacing the isotropic magnetic interaction and the isotropic g factor of Fe^{2+} with anisotropic tensors, to describe the EPR spectra of $Q^- Fe^{2+}$. The resulting spin Hamiltonian is

$$\mathcal{H} = D[(S_{Fe,z}^2 - \tfrac{1}{3} S_{Fe}(S_{Fe} + 1)] + (E/D)(S_{Fe,x}^2 - S_{Fe,y}^2)] + \mu_B \mathbf{H} \cdot \mathbf{g}_{Fe} \cdot \mathbf{S}_{Fe} + g_Q \mu_B \mathbf{H} \cdot \mathbf{S}_Q - \mathbf{S}_{Fe} \cdot \mathbf{J} \cdot \mathbf{S}_Q, \tag{11}$$

where D and E/D are the Fe^{2+} crystal field parameters, $\mathbf{g}_{Fe}$ is the Fe^{2+} g tensor, g_Q is the isotropic Q^- g factor, $\mathbf{J}$ is the magnetic interaction tensor, $\mathbf{S}_{Fe}$ and $\mathbf{S}_Q$ are the spin operators for Fe^{2+} and Q^-, respectively, μ_B is the Bohr magneton and $\mathbf{H}$ is the external magnetic field.

The $Q^- Fe^{2+}$ complex has $(2S_{Fe} + 1)(2S_Q + 1) = 10$ states, whose energy levels are the eigenvalues of $\mathcal{H}$. In the absence of an external magnetic field, these levels are doubly degenerate, with energies E_i; $i = 1, \ldots, 5$, in increasing order. The spacings of the doublet levels are determined by the crystal field acting on Fe^{2+}, modified slightly by the magnetic interaction with Q^-. The first excited doublet is ~3 K above the ground doublet, the next higher doublet is ~15 K above the ground doublet (Fig. 7). In the presence of an external magnetic field these doublets

[7] In Butler et al., 1980, we considered only exchange interactions; in this paper, whenever we use the term magnetic interaction we include dipolar interactions as well.

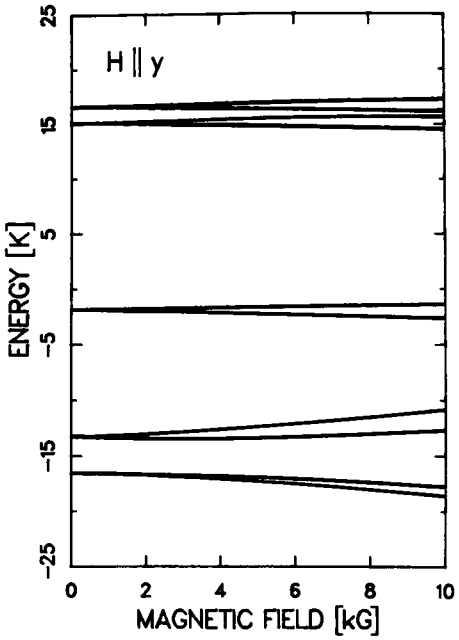

FIGURE 7 Energy levels of the Hamiltonian, Eq. 11, for the Q^-Fe^{2+} complex, vs. magnetic field, for the field in the y direction. The parameters deduced from the magnetization measurements (Butler et al., 1980) were used (D = 7.60 K, E/D = 0.25, isotropic g_{Fe} = 2.16, and isotropic J = −0.29 K). The levels for the other principal axes are shown in Butler et al., 1980, Fig. 3.

split, the split levels corresponding roughly to spin up, ↑, and spin down, ↓, of the unpaired electron on Q^-. The frequency of the microwave field (9 GHz corresponds to 0.43 K) is too low to induce transitions between the separate doublets. Transitions occur only within the doublets.

For the sake of intuitive understanding of the EPR spectrum, we present first an elementary discussion that relies only on the relatively small energy separation of the lowest two doublets and some properties of the Fe^{2+} magnetization known from (Butler et al., 1980). Then we present a more systematic perturbation calculation, and finally we discuss an exact numerical analysis of the EPR spectrum derived from the spin Hamiltonian.

Elementary Treatment

We begin by considering QFe^{2+}, i.e., the unreduced acceptor complex. There are five states (i = 1, . . ., 5) of Fe^{2+}, with energies E_i. The magnetic moment of each of these states is zero in the absence of an external magnetic field. Application of an external field causes weak mixing of the five states, giving rise to magnetic moments proportional to the field. The induced moment of the ground state is responsible for the low-temperature magnetization discussed in Butler et al., 1980. These induced magnetic moments, $m_{i,Fe}$, can be written as

$$m_{i,Fe} = \alpha_i H, \tag{12}$$

where α_i is the Fe^{2+} magnetic polarizability. The relation between magnetic moment and field is strongly anisotropic, as discussed in Butler et al., 1980. The y-axis is an "easy" axis of magnetization, meaning $m_{1,Fe}$ and $m_{2,Fe}$ are much larger for H parallel to the y-axis than for other directions of H. This is because $m_{1,Fe}$ and $m_{2,Fe}$ arise primarily from mixing of the states 1 and 2, which have a small energy difference, when H is parallel to the y-axis, as opposed to mixing of state 1 with the much higher energy states 3 and 4 for H in the xz-plane. For simplicity, we shall ignore the higher energy states in this section. Accordingly, $m_{1,Fe}$ and $m_{2,Fe}$ will be regarded as zero for H perpendicular to the y-axis. With the restriction to only two states, $\alpha_1 \geq 0$ and $\alpha_2 \leq 0$, i.e., the ground state magnetization is parallel to the field and the excited state magnetization is anti-parallel.[8]

When the acceptor complex is singly reduced (Q^-Fe^{2+}), the added electron on Q^- has spin 1/2, giving rise to degenerate doublets, with energy difference $E_{ij} = E_i - E_j$

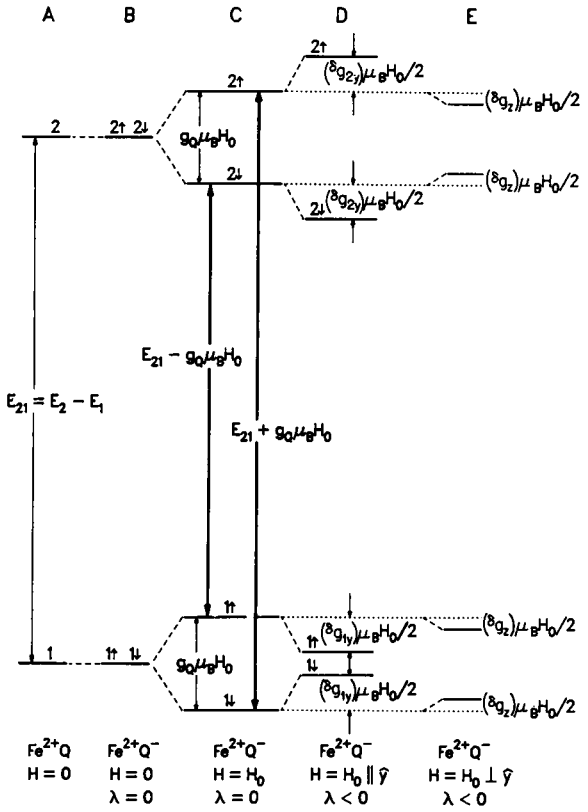

FIGURE 8 Energy levels of the two lowest doublets of Q^-Fe^{2+} showing effects of magnetic field, H, and magnetic interaction, λ, between Fe^{2+} and Q^-, as discussed in the elementary treatment. Each level is labeled with its state(s), and each of the splittings is labeled. The heavy arrows show the states connected by the magnetic interaction λ.

[8]This is apparent from Fig. 2 of Butler et al., 1980 (and Fig. 7 of this paper) where, for H in the y direction, the ground state energy curves down, $\alpha_1 > 0$, and the excited state energy curves up, $\alpha_2 < 0$, for increasing H. (Note that $m_{i,Fe} = \partial E_i/\partial H$.)

between them. This is illustrated in Figs. 8 *A* and 8 *B* for the lowest two doublets. The application of an external magnetic field splits each of these doublets. If there were no magnetic interaction between Q^- and Fe^{2+}, the EPR spectrum would be exactly as in iron-free RCs, with a single sharp resonance at $g_Q = 2.0046$ (Feher et al., 1972) (see Fig. 8 *C*). We know however, from Butler et al., 1980, that there is a magnetic interaction between Q^- and Fe^{2+}, which can be described roughly as an internal magnetic field H_{int} acting on Q^-. It depends on the state, i, of Fe^{2+} and is given by

$$H_{int} = \lambda m_{i,Fe} = \lambda \alpha_i H. \tag{13}$$

The internal field combines with the externally applied field to produce an effective field H_{eff}. Thus the resonance condition at the microwave frequency ν is given by

$$h\nu = g_Q \mu_B H_{eff} = g_Q \mu_B [H + \lambda m_{i,Fe}] = g_Q [1 + \lambda \alpha_i] \mu_B H. \tag{14}$$

Thus, for H parallel to the y-axis, the EPR transitions will have g values given by

$$g_{i,y} = g_Q [1 + \lambda \alpha_i]. \tag{15}$$

For H perpendicular to the y-axis there is no internal field and consequently no change in the g value i.e.,

$$g_{i,x} = g_{i,z} = g_Q. \tag{16}$$

From the static magnetization measurements in Butler et al., 1980, we determined an antiferromagnetic interaction ($\lambda < 0$), i.e., the effective g value of Q^- was reduced by the Fe^{2+}. Consequently, the Zeeman energy of the ground state ($i = 1$) is reduced (see Fig. 8 *D*).

The effective g values g_i (Eqs. 15 and 16) determine the shape of the EPR spectrum. Since the RCs in our samples are randomly oriented with respect to the magnetic field, the EPR line will be broadened inhomogeneously, reflecting the spread in g values for different orientations. Because there are more orientations with H in the xz-plane than perpendicular to it, the EPR spectrum for both the ground doublet and the excited doublet should peak at $g = g_Q$ (Eq. 16) and taper off towards $g_{i,y}$ (Eq. 15). Since the sign of α is opposite for the ground and excited doublets, the g shifts for the two doublets are in opposite directions (see Eq. 15), giving rise to the spectrum sketched in Fig. 9 *A*. In this sketch we have assumed equal intensities for all the transitions and have ignored the thermal population differences of the two doublets.

Our discussion so far, which is equivalent to first-order perturbation theory in λ, suggests that there should be no g shift for the magnetic field along the x- and z-axes. In fact, there is a shift of second order in λ involving the two lowest doublets. The second-order shift in the energy E of a level is given by (Schiff, 1968)

$$\delta E = \frac{|\mathrm{ME}|^2}{E - E_i}, \tag{17}$$

where E_i is the energy of an intermediate state, ME is the matrix element, and $|\mathrm{ME}|$ is appropriate for the virtual transition to that state. The only allowed transitions among the four levels of the lowest two doublets are those labeled with heavy arrows in Fig. 8. These transitions have the same matrix element, given by[9]

$$|\mathrm{ME}| \approx \lambda g_Q g_{Fe} \mu_B^2 = J. \tag{18}$$

The energy denominators differ by $2g_Q\mu_B H_0$ (Fig. 8 *C*). Substituting the energy shifts into Eq. 17 (see Fig. 8 *C*), we obtain for $H_0 \perp y$-axis

$$\begin{aligned} E_{1\uparrow} - E_{1\downarrow} &= g_Q \mu_B H_0 + \delta E_{1\uparrow} - \delta E_{1\downarrow} \\ &= g_Q \mu_B H_0 - \frac{|\mathrm{ME}|^2}{E_{21} - g_Q \mu_B H_0} + \frac{|\mathrm{ME}|^2}{E_{21} + g_Q \mu_B H_0} \\ &= g_Q \left(1 - \frac{2|\mathrm{ME}|^2}{E_{21}^2}\right) \mu_B H_0, \end{aligned} \tag{19}$$

with the same result for the energy shifts of the second doublet (see Fig. 8 *E*). Substituting for $|\mathrm{ME}|$ from Eq. 18, we obtain for the resultant g values of both doublets

$$g_{i,x} = g_{i,z} = g_Q \left[1 - 2\left(\frac{\lambda g_Q g_{Fe} \mu_B^2}{E_{21}}\right)^2\right] = g_Q \left[1 - 2\left(\frac{J}{E_{21}}\right)^2\right]. \tag{20}$$

Since we know from Butler et al., 1980 that $E_{21} \approx 3$ K and from this work that the spectrum peaks at $g = 1.8$, we predict from Eq. 20 an exchange interaction $|J| \approx 0.7$ K. This value is consistent with the results of Butler et al., 1980. Thus, the spectrum predicted by the elementary treatment already has features characteristic of the observed spectra, i.e., a peak at $g = 1.8$ with broad wings extending to both large and small g values (see Fig. 9 *A*). Since the g values (Eqs. 15 and 20) do not depend on the microwave frequency ν, this treatment also explains the frequency dependence of the observed spectra.

Higher-Order Perturbation Treatment

The elementary treatment above produced effective g values (Eqs. 15 and 20) to the lowest order in the magnetic interaction within the two lowest doublets. The resulting spectrum is suggestive of the observed spectrum, but predicts neither as wide a central peak as is observed, nor the observed temperature dependence of the central peak. To keep the elementary treatment simple, we neglected first-order terms involving the third and higher doublets. We shall now include these terms as well as second-order terms within the two lowest doublets.

When we apply degenerate perturbation theory to the ith doublet, we find an effective Hamiltonian $\mathcal{H}_i$ in the Q^-

[9]This can be seen by writing an isotropic interaction term in the spin Hamiltonian (Eq. 11) as $J\mathbf{S}_{Fe} \cdot \mathbf{S}_Q = \lambda \mathbf{m}_{Fe} \cdot \mathbf{m}_Q = \lambda g_{Fe} \mu_B \mathbf{S}_{Fe} \cdot g_Q \mu_B \mathbf{S}_Q$, i.e., $J = \lambda g_{Fe} g_Q \mu_B^2$.

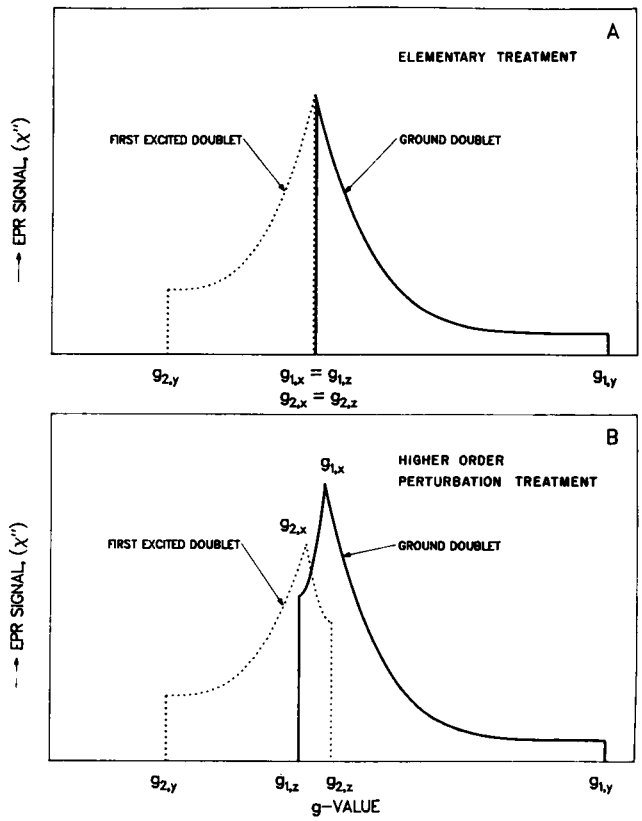

FIGURE 9 Sketches of EPR spectra expected for the lowest two doublets of the Q^-Fe^{2+} complex based on elementary and detailed perturbation treatments described in the text. (*A*) The elementary treatment predicts coincident peaks at the g value $g_{i,x} = g_{i,z}$ of each doublet i (=1,2), with a low-field edge at $g_{2,y}$ and a high-field edge at $g_{1,y}$. For $J_y > 0$, the two spectra would be flipped around, with the ground doublet spectrum on the low-field side. (*B*) The complete perturbation treatment predicts $g_{i,x} \neq g_{i,z}$, producing a wider central peak resembling the observed spectrum. The sketches in *A* and *B* do not consider transition probabilities or temperature (see text).

spin space; it has the form

$$\mathcal{H}_i = E_i' + \mu_B \mathbf{H} \cdot \mathbf{g}_i \cdot \mathbf{S}_Q, \tag{21}$$

where $\mathbf{g}_i$ is the effective g tensor for the ith doublet and $E_i' = E_i$ + field-independent terms and field-dependent but S_Q-independent terms from the perturbation. We know from the elementary discussion that we must compute $\mathbf{g}_i$ to at least order J^2 to obtain the main features of the observed EPR signal, so we must calculate $\mathcal{H}_i$ to third order. These calculations are described in Appendix A. For simplicity, we shall restrict ourselves to diagonal $\mathbf{J}$ and $\mathbf{g}_{Fe}$. The calculated g tensors will then also be diagonal.[10]

Table IIA presents the resultant g values for the principal axis directions for the two lowest doublets, with Table IIB presenting the nonzero matrix elements and other quantities used in Table IIA. The columns of this Table present the zeroth order g value, the first-order g shift, and the second-order g shift in two parts, as described in Appendix A. Within each row, the first line gives the full expression for the term, the second line gives the numerical result parameterized by J for particular values of D and E (D = 7.60 K, E/D = 0.25), and the third line gives the numerical result for a particular $\mathbf{J}$ (J_x = −0.13 K, J_y = −0.58 K, J_z = −0.58 K). The accumulated g values are presented in the last column. The elementary treatment explained terms in $\delta g_i^{(1)}$ and $\delta g_i^{(2a)}$, although the expressions were approximate since only terms within the lowest two doublets were considered.

From Table IIA, we see that even in first-order $g_{i,x} \neq g_{i,z}$ for either doublet (i = 1,2). This inequality produces an additional width of the central peak as shown in the sketch of Fig. 9 *B*. In this sketch, we have again assumed equal intensities for all transitions and have ignored thermal population differences of the two doublets. If thermal populations were taken into account, the amplitude of the low-field side of the spectrum would increase with increasing temperature, as is observed experimentally (e.g., see Fig. 4).

Although the above treatment qualitatively explains the salient features of the spectrum, one encounters some quantitative difficulties, notably with the expressions for $g_{i,y}$. If we use the value of J_y obtained either from the elementary treatment (J_y = −0.7 K) or from the numerical treatment to be discussed later (J_y = −0.58 K), the calculated value of $g_{1,y}$ is negative—a nonsensical result (see Table IIA) showing that perturbation theory fails for $\delta g_{1,y}^{(1)}$. This problem does not arise for $\delta g_{1,x}^{(1)}$ and $\delta g_{1,z}^{(1)}$.

A possible cure, within the framework of perturbation theory, would be to use "almost degenerate" perturbation theory, taking the lowest two doublets as the manifold of unperturbed states. We would obtain a spin Hamiltonian for a fictitious spin of 3/2, which we could solve exactly. Daunted by the complexities of this method and by the complexity of calculating the line shape (including matrix elements for the transitions induced by the microwave field) even for our simple perturbation theory, we undertook instead an exact numerical treatment of the spin Hamiltonian (Eq. 11) as described in the next section.

To provide initial guidance in the choice of the parameters of $\mathcal{H}$ for the numerical treatment, we used the perturbation results and the following assumption: for each doublet, $g_{i,x}$ and $g_{i,z}$ flank the peak of the spectrum (see Fig. 9 *B*). A reasonable requirement, therefore, is that the average of $g_{i,x}$ and $g_{i,z}$ equal the experimentally observed g value, i.e.,

$$\tfrac{1}{2}(g_{i,x} + g_{i,z}) = 1.80, \qquad i = 1, 2. \tag{22}$$

Using the values of D, E, and $\mathbf{g}_{Fe}$ deduced from the

[10]We consequently refer to the elements of these tensors with a single subscript, x, y, or z, where we mean the corresponding diagonal elements of the tensors, xx, yy, or zz.

TABLE IIA
g-VALUES ALONG PRINCIPAL AXES FOR LOWEST TWO DOUBLETS*

	$g_i^{(0)}$	$\delta g_i^{(1)}$	$\delta g_i^{(2a)}$	$\delta g_i^{(2b)}$	g_i
$g_{1,x}$	g_Q	$\frac{2Q^2}{E_{31}} J_x g_{Fe,x}$	$-\frac{g_Q}{2}\left[\frac{J_y^2P^2}{E_{21}^2}+\frac{J_z^2(P+Q)^2}{E_{41}^2}\right]$	$g_{Fe,x}J_yJ_z\left[\frac{P(P+Q)}{E_{21}E_{41}}-\frac{Q(P+Q)}{E_{31}E_{41}}+\frac{PQ}{E_{21}E_{31}}\right]$	
	2.00	$0.660J_x$	$-0.339J_y^2-0.0002J_z^2$	$2.16[0.007+0.002-0.059]J_yJ_z$	
	2.00	-0.095	-0.114	-0.036	1.76
$g_{1,y}$	g_Q	$\frac{2P^2}{E_{21}} J_y g_{Fe,y}$	$-\frac{g_Q}{2}\left[\frac{J_x^2Q^2}{E_{31}^2}+\frac{J_z^2(P+Q)^2}{E_{41}^2}\right]$	$g_{Fe,y}J_zJ_x\left[\frac{Q(P+Q)}{E_{31}E_{41}}+\frac{PQ}{E_{21}E_{31}}-\frac{P(P+Q)}{E_{21}E_{41}}\right]$	
	2.00	$5.016J_y$	$-0.010J_x^2-0.0002J_z^2$	$2.27[-0.002-0.059-0.007)J_zJ_x$	
	2.00	-2.909	0.000	-0.013	-0.92
$g_{1,z}$	g_Q	$\frac{2(P+Q)^2}{E_{41}} J_z g_{Fe,z}$	$-\frac{g_Q}{2}\left[\frac{J_x^2Q^2}{E_{31}^2}+\frac{J_y^2P^2}{E_{21}^2}\right]$	$g_{Fe,z}J_xJ_y\left[-\frac{PQ}{E_{21}E_{31}}-\frac{P(P+Q)}{E_{21}E_{41}}-\frac{Q(P+Q)}{E_{31}E_{41}}\right]$	
	2.00	$0.021J_z$	$-0.010J_x^2-0.339J_y^2$	$2.04[0.059-0.007+0.002]J_xJ_y$	
	2.00	-0.012	-0.114	0.009	1.88
$g_{2,x}$	g_Q	$\frac{2}{E_{42}} J_x g_{Fe,x}$	$-\frac{g_Q}{2}\left[\frac{J_y^2P^2}{E_{21}^2}+\frac{J_y^2S^2}{E_{32}^2}+\frac{J_z^2}{E_{32}^2}\right]$	$g_{Fe,x}J_yJ_z\left[-\frac{RS}{E_{32}E_{52}}+\frac{PQ}{E_{21}E_{32}}+\frac{P(P+Q)}{E_{21}E_{42}}+\frac{1}{E_{32}E_{42}}-\frac{(R+S)S}{E_{42}E_{52}}\right]$	
	2.00	$0.152J_x$	$-(0.339+0.0004)J_y^2-0.008J_z^2$	$2.16[-0.002-0.059+0.007+0.003-0.001]J_yJ_z$	
	2.00	-0.021	-0.117	-0.038	1.82
$g_{2,y}$	g_Q	$\left[-\frac{2P^2}{E_{21}}+\frac{2S^2}{E_{52}}\right] J_y g_{Fe,y}$	$-\frac{g_Q}{2}\left[\frac{J_x^2}{E_{42}^2}+\frac{J_z^2}{E_{32}^2}\right]$	$g_{Fe,y}J_zJ_x\left[-\frac{1}{E_{32}E_{42}}+\frac{RS}{E_{32}E_{52}}-\frac{PQ}{E_{21}E_{32}}+\frac{P(P+Q)}{E_{21}E_{42}}-\frac{(R+S)S}{E_{42}E_{52}}\right]$	
	2.00	$-4.956J_y$	$-0.001J_x^2-0.008J_z^2$	$2.27[-0.003+0.002+0.059+0.007-0.001)J_zJ_x$	
	2.00	2.874	-0.003	0.012	4.88
$g_{2,x}$	g_Q	$\frac{2}{E_{32}} J_z g_{Fe,z}$	$-\frac{g_Q}{2}\left[\frac{J_x^2}{E_{42}^2}+\frac{J_y^2P^2}{E_{21}^2}+\frac{J_y^2S^2}{E_{52}^2}\right]$	$g_{Fe,z}J_xJ_y\left[-\frac{P(P+Q)}{E_{21}E_{42}}+\frac{(R+S)S}{E_{42}E_{52}}+\frac{RS}{E_{32}E_{52}}-\frac{PQ}{E_{21}E_{32}}+\frac{1}{E_{32}E_{42}}\right]$	
	2.00	$0.358J_z$	$-0.001J_x^2-0.339J_y^2$	$2.04[-0.007+0.001+0.002+0.059+0.003]J_xJ_y$	
	2.00	-0.208	-0.114	0.010	1.69

*All tensors are taken to be diagonal; single subscripts x, y, z refer to xx-component, etc.
$\mathbf{g}_i$ is the effective g-tensor for i^{th} doublet.
$g_i^{(0)}$ is the zero-order result for the g-value. $\delta g_i^{(1)}$ is the first order g-shift. $\delta g_i^{(2a)}$ and $\delta g_i^{(2b)}$ are second order g-shifts.
$\mathbf{g}_{Fe}$ is the Fe^{2+} g-tensor; g_Q is the quinone g-value.
$\mathbf{J}$ is the magnetic interaction tensor.
E_{ij} is the zero-field energy difference between doublets i and j.
P, Q, R, and S are expressions appearing in the matrix elements of $\mathbf{S}_{Fe}$, these matrix elements are summarized in Table IIb.
First line for each g-component is the perturbation expression; second line is evaluated for D, E and $\mathbf{g}_{Fe}$ given by Eqs. 23a,b; third line is evaluated for $\mathbf{J}$ given by Eq. 23c.

magnetization measurements, we evaluated the largest perturbation terms for $g_{i,x}$ and $g_{i,z}$ (see Table IIA). Substituting these terms in Eq. 22 results in two equations relating J_x, J_y, and J_z. For a given J_y, the two equations are solved for J_x and J_z; Fig. 10 presents the results. Because anisotropies of exchange interactions are generally small (Abragam and Bleaney, 1970), we looked for a nearly isotropic tensor $\mathbf{J}$ that satisfied Eq. 22.[11] The dashed diagonal line in Fig. 10 is the locus of isotropic $\mathbf{J}$. We made $|J_x - J_y| = |J_z - J_y|$ by picking the intersection points on the vertical line. This gives the values: $J_x = -0.36$ K, $J_y = -0.45$ K, $J_z = -0.55$ K.

[11]Fig. 10 only shows $J_y < 0$. J_x and J_z are approximately even functions of J_y. Thus for any reasonably small J_y, J_x and J_z are both negative for either sign of J_y. To make $\mathbf{J}$ as isotropic as possible we consider negative J_y.

Numerical Treatment

Our approach to the numerical calculation of the EPR spectrum of Q^-Fe^{2+} supposes that the characteristic shape of the spectrum results from averaging the individual spectra of randomly oriented RCs in frozen solution, as described in the elementary treatment. We developed numerical procedures to solve for the energy levels of $\mathcal{H}$ (Eq. 11), from which the resonance fields and the transition intensities for given orientations of RCs were found. The simulated spectra were obtained by averaging the resulting line spectra over all orientations of the RC. These calculations are outlined below and described in detail in Appendix B.

The energy levels of Q^-Fe^{2+} are the eigenvalues of $\mathcal{H}$, which were computed as described in Butler et al., 1980 for a given set of values of D, E, $\mathbf{g}_{Fe}$ and $\mathbf{J}$. Fig. 11 shows the energy levels of the lowest two doublets as a function of the

TABLE IIB
MATRIX ELEMENTS OF S_{Fe} BETWEEN Fe^{2+} STATES

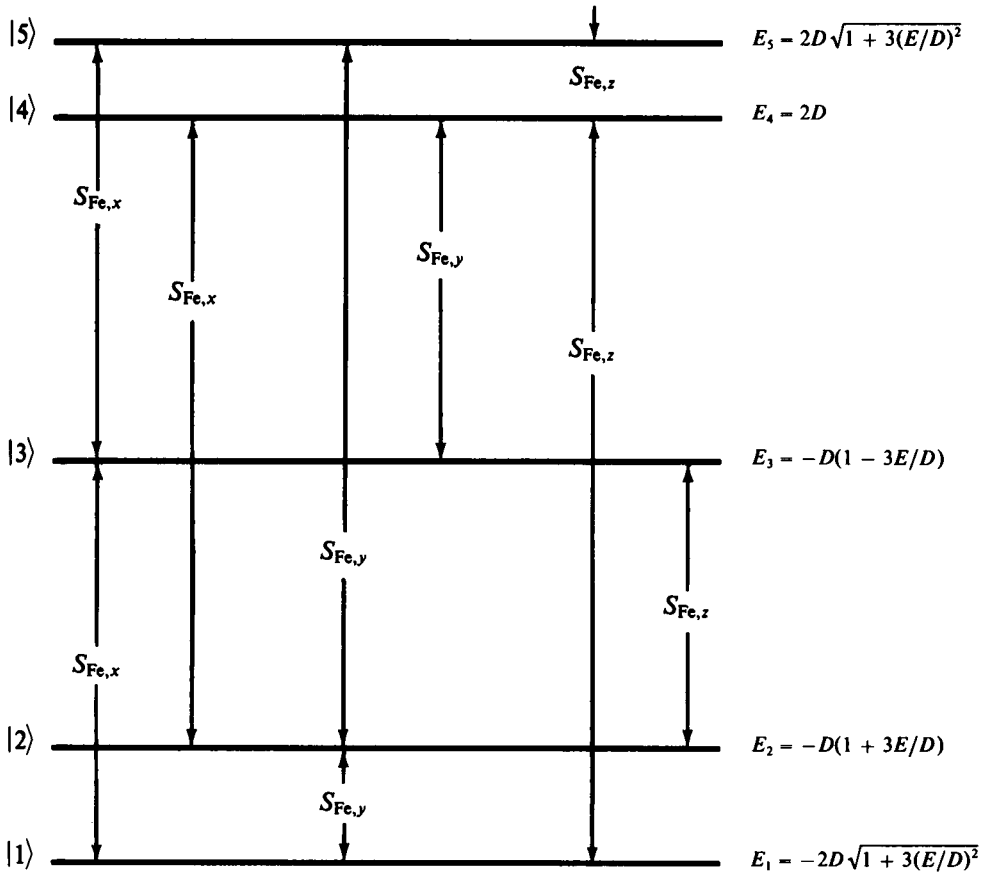

$$\langle 3|S_{Fe,x}|1\rangle = Q \quad \langle 2|S_{Fe,y}|1\rangle = iP \quad \langle 4|S_{Fe,z}|1\rangle = P + Q$$
$$\langle 5|S_{Fe,x}|3\rangle = R \quad \langle 5|S_{Fe,y}|2\rangle = iS \quad \langle 5|S_{Fe,z}|4\rangle = R + S$$
$$\langle 4|S_{Fe,x}|2\rangle = 1 \quad \langle 4|S_{Fe,y}|3\rangle = -i \quad \langle 3|S_{Fe,z}|2\rangle = 1$$

$$P = \frac{\sqrt{1 + 3(E/D)^2} - 1 + 3E/D}{[(\sqrt{1 + 3(E/D)^2} - 1)^2 + 3(E/D)^2]^{1/2}}$$
$$Q = \frac{\sqrt{1 + 3(E/D)^2} - 1 - 3E/D}{[(\sqrt{1 + 3(E/D)^2} - 1)^2 + 3(E/D)^2]^{1/2}}$$
$$R = \frac{\sqrt{1 + 3(E/D)^2} + 1 + 3E/D}{[(\sqrt{1 + 3(E/D)^2} + 1)^2 + 3(E/D)^2]^{1/2}}$$
$$S = \frac{\sqrt{1 + 3(E/D)^2} + 1 - 3E/D}{[(\sqrt{1 + 3(E/D)^2} + 1)^2 + 3(E/D)^2]^{1/2}}$$

applied field H, for H directed along each of the principal axes. For a particular direction of the static field, the resonance condition is satisfied at a magnetic field at which the doublet splitting equals the incident microwave frequency. The positions of these resonances are shown in Fig. 11 for 9 GHz. They span g values from 0.62 to 4.68, and tend to cluster around $g = 1.8$. Calculation of the EPR spectrum requires knowledge of the eigenstates in addition to the energy eigenvalues for all directions of the static field.

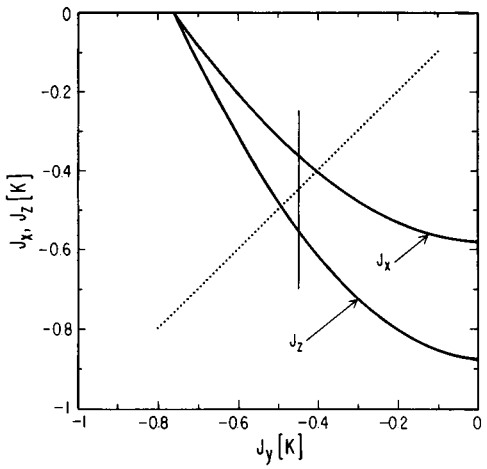

FIGURE 10 Illustration of the procedure for choosing initial value of **J** for numerical calculation of EPR spectrum. J_x and J_z are plotted vs. J_y such that Eqs. 22 are satisfied. Dotted line represents locus of isotropic **J**. We chose as nearly an isotropic **J** as possible by requiring $|J_x - J_y| = |J_z - J_y|$, as indicated by the vertical line. The values of J_x and J_z are obtained from the intercepts of the vertical line with the respective curves.

The Zeeman interaction of the Q^- and Fe^{2+} spins with the microwave radiation field induces the resonance transitions. Since this interaction is small (the radiation field is typically <1 G), time-dependent perturbation theory was used to calculate the intensities of the line spectra of the five doublets for a given orientation of an RC. These intensities were averaged with respect to RC orientation to yield the predicted EPR spectrum in the absence of a true line width. A computer program was developed to evaluate this "powder" averaged spectrum for each doublet (for details see Appendix B). The spectra were calculated at 8-G intervals from 0 to 8 kG. When these spectra were plotted by connecting the calculated points, sharp discontinuities appeared. To eliminate them, we smoothed the spectrum by convolving it with a Gaussian having a half width at half maximum of 20 G. This procedure did not remove any structure that was within experimental resolution (see Fig. 2, inset, dotted curve).

Using the values of **J** obtained from perturbation theory, the simulated spectra shown in Fig. 12 were obtained. Their general shape is similar to but not identical with that obtained from perturbation theory (Fig. 9 *B*); the most noticeable difference is in the position of the low-field edge at $g_{2,y}$. The perturbation calculation predicts that $g_{2,y}$ depends monotonically on J_y (see Table IIA). The numerical calculation confirms this behavior for $g_{2,y} < 4.6$, but further increases in $|J_y|$ do not increase $g_{2,y}$. For sufficiently large $|J_y|$, $g_{2,y}$ even decreases, which points out the failure of the perturbation treatment when $|J_y|$ becomes comparable with the energy splitting E_{21} between the two lowest doublets.

The temperature dependence of the spectrum was obtained by adding the spectra of the two lowest doublets with the appropriate Boltzmann weighting factor. The spin Hamiltonian parameters were varied to optimize the agreement with experimentally observed spectra, as described in the next section.

DETAILED COMPARISON OF THEORY WITH EXPERIMENT

In this section we shall compare quantitatively the main features of the observed spectra with those predicted by the theory developed in the previous section. In view of the enhanced resolution of the EPR spectra in the presence of *o*-phenanthroline we shall start with the spectra obtained from sample No. 2 (see Table I and Fig. 4 *B*) and consider RCs in other environments later.

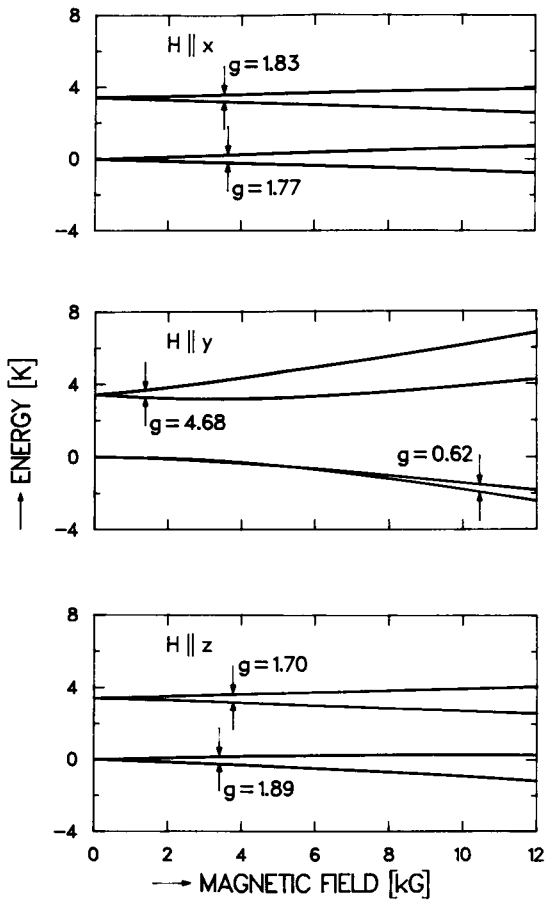

FIGURE 11 The lowest four energy levels of the Q^-Fe^{2+} complex vs. applied magnetic field for the field parallel to the principal axes. The levels occur as Kramers doublets and were numerically calculated from the Hamiltonian Eq. 11, using the parameters $D = 7.60$ K, $E/D = 0.25$, $g_{Fe,x} = 2.16$, $g_{Fe,y} = 2.27$, $g_{Fe,z} = 2.04$, $J_x = -0.13$ K, $J_y = -0.58$ K, $J_z = -0.58$ K (see Eq. 23). The positions at which EPR transitions are expected to occur at 9.0 GHz are indicated. The Fe^{2+} parameters D, E, and $\mathbf{g}_{Fe}$ are those deduced from the magnetization results of Butler et al, 1980. (In Butler et al., 1980 an isotropic J was assumed; consequently the positions of the transitions were predicted to occur at different fields from those shown here.)

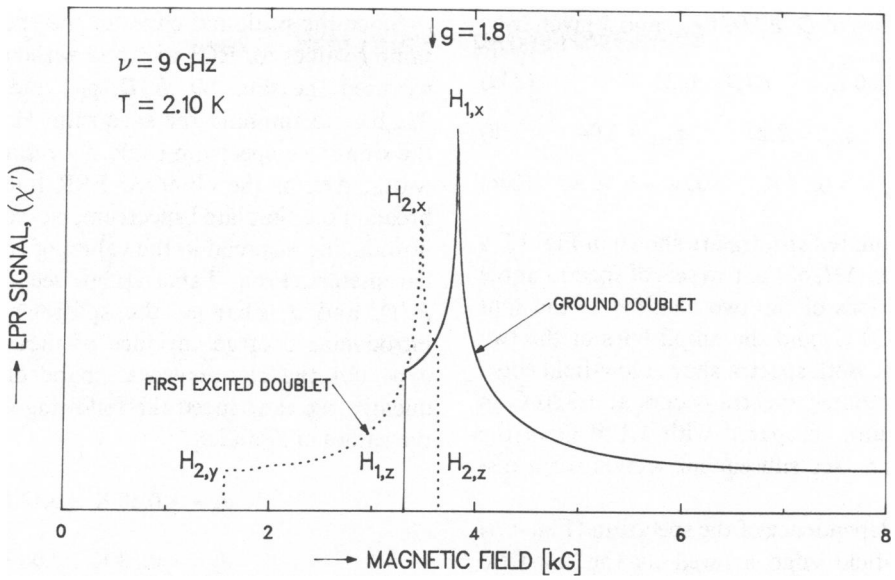

FIGURE 12 Simulated EPR spectrum of each of the lowest two doublets, of the Q^-Fe^{2+} complex weighted by the appropriate Boltzmann factors for $T = 2.1$ K. The diagonal magnetic interaction $J_x = -0.36$ K, $J_y = -0.45$ K, $J_z = -0.55$ K, deduced from Fig. 10 was used; the Fe^{2+} parameters are given by Eqs. 23a,b. $H_{i,j}$'s identify key features, with $i = 1,2$ labeling the doublet and $j = x, y, z$ labeling the feature, analogous to the g value labels of Fig. 9. Note that x, y, z in this case are simply labels and do not necessarily imply that the external magnetic field lies exactly along that axis, as was strictly true for Fig. 9. Qualitatively similar spectra were obtained by using the parameters of Eq. 23 (see Fig. 14).

EPR Lineshape

Five parameters are required to produce a numerical simulation of the EPR spectrum. These are D, E/D, $\mathbf{g}_{Fe}$, $\mathbf{J}$ (see Eq. 11), and the temperature T. Three parameters, D, E/D, and $\mathbf{g}_{Fe}$, were obtained from magnetization measurements (in Butler et al., 1980, see Table II, sample RT1). Their values are given by Eqs. 23a,b, where $\mathbf{g}_{Fe}$ was obtained by scaling the anisotropies predicted by theoretical considerations (in Butler et al., 1980, see Appendix A) to the (rms) g value determined for RT1 (in Butler et al., 1980, see Table II). Using the initial value of $\mathbf{J}$ obtained from perturbation calculations, we produced simulated spectra, (e.g., Fig. 12), that qualitatively resembled the observed spectra but quantitatively provided relatively poor simulations. Consequently, we searched for a $\mathbf{J}$ to improve the simulation. Four comparison criteria were used to optimize the agreement of the numerical simulation with the observed spectra: (*a*) The width of the spectrum, ΔH (Fig. 1); (*b*) The position of the maxima of the split peak (inset, Fig. 2); (*c*) The temperature dependence of the overall shape (Fig. 4); and (*d*) The position of the low-field edge (at $g = 5.5$ in Fig. 4 *B*).

The numerically simulated spectra exhibit features (see Fig. 12) similar to those observed: (*a*) the two maxima of the peak occur at $H_{1,x}$ and $H_{2,x}$, (*b*) the extrema of the $d\chi''/dH$ spectra occur at $H_{1,z}$ and $H_{2,z}$, corresponding to g_1 and g_2 of Fig. 1 *B*, (*c*) the low-field edge occurs at $H_{2,y}$. To aid our search for $\mathbf{J}$ that optimizes the simulations, we determined the sensitivities of these features to variations in each of the spin Hamiltonian parameters. Table III summarizes the changes in $H_{i,j}$ for 10% changes in D, E/D, J_x, J_y, and J_z. Varying D or E/D affects both the line width δH ($H_{2,z} - H_{1,z}$) and the maxima splitting of the peak ($H_{1,x} - H_{2,x}$), varying J_x changes the maxima splitting with little effect on δH, varying J_y has little effect on either quantity, and varying J_z changes δH with little effect on the maxima splitting. The low-field edge $H_{2,y}$ is predominantly affected by the value of J_y.

RCs with o-Phenanthroline. A simulation that approximately satisfied the four criteria mentioned earlier

TABLE III
PERCENT CHANGE IN H_{ij} FOR ±10% CHANGE IN A SPIN HAMILTONIAN PARAMETER

Feature	Spin Hamiltonian Parameter						
	D		E/D		$\lvert J_x\rvert$	$\lvert J_y\rvert$	$\lvert J_z\rvert$
	−10%	+10%	−10%	+10%	±10%	±10%	±10%
$H_{1,x}$	+1.6	−2.1	−.28	.88	±.51	±1.2	±.22
$H_{2,x}$	+1.0	−1.5	−.57	+1.3	±.10	±1.3	±.28
$H_{1,z}$	+.74	−1.1	−1.3	+1.3	∓.03	±1.0	±.09
$H_{2,z}$	+1.6	−2.6	−.05	+.05	∓.05	±1.0	±1.1
$H_{2,y}$	−4.6	+4.6	+3.0	−3.0	∓.07	∓4.6	±.10
$H_{1,x} - H_{2,x}$§	+18.	−20.	+9.0	−13.	±13.	±0.0	∓1.7
$H_{2,z} - H_{1,z}$‖	+10.	−14.	+12.	−12.	∓.30	±1.4	±11.

*The sensitivities were calculated for a microwave frequency of 9 GHz using the values for the parameters given by Eqs. 23a,b,c.
‡For the definition of $H_{i,j}$ see Fig. 12.
§$H_{1,x} - H_{2,x}$ is the splitting of the maxima of the peak.
‖$H_{2,z} - H_{1,z}$ is interpreted as the linewidth δH.

was found for the values of D, E/D,[12] $\mathbf{g}_{Fe}$, and $\mathbf{J}$ given by

$$D = 7.60 \text{ K}, \qquad E/D = 0.25 \tag{23a}$$

$$g_{Fe,x} = 2.16, \qquad g_{Fe,y} = 2.27, \qquad g_{Fe,z} = 2.04. \tag{23b}$$

$$J_x = -0.13 \text{ K}, \qquad J_y = -0.58 \text{ K}, \qquad J_z = -0.58 \text{ K}. \tag{23c}$$

The observed and simulated spectra are shown in Fig. 13 *A* and *B*. The line widths, ΔH, of the two sets of spectra agree within 10%, the positions of the two maxima of the split peak agree within ±20 G, and the amplitudes of the two maxima within ≲20%. Both spectra show a low-field edge; its position in the simulated spectra occurs at 1,380 G in the simulated spectrum, compared with 1,150 G in the experimental spectrum (see subsequent section for a discussion).

The temperature dependence of the spectrum (Fig. 4 *B*) shows that the low-field edge as well as the low-field maximum of the split peak increases with temperature. This is a consequence of an anti-ferromagnetic interaction ($J < 0$), which requires that the low-field part of the EPR line is due to the excited doublet as shown in Fig. 9 (for a ferromagnetic interaction the positions of the ground and excited doublets in Fig. 9 would be reversed). Thus we have shown that for sample No. 2 our theory explains features *a*, *c*, and *d* (stated at the end of the Experimental section).

RCs without o-Phenanthroline. The observed spectra for RCs without *o*-phenanthroline are broader and less well resolved than those with *o*-phenanthroline (compare Figs. 4 *A* and 4 *B* and Table I). Although the peak is not resolved into separate maxima, there are two edges of the peak with an intervening plateau (Fig. 2, inset). The relative amplitudes of the two edges vary with temperature in a manner similar to the variation of the maxima in RCs with *o*-phenanthroline. The low-field edge, at ~1.2 kG, is much broader than for RCs with *o*-phenanthroline, but it also shows an increase in amplitude with increasing temperature.

[12]The use of these values needs to be justified in view of the smaller values for D and E/D reported in Butler et al., 1980 when *o*-phenanthroline was present in an unreduced sample. Besides the fact that the same D and E/D produces the best EPR simulations for RCs with or without *o*-phenanthroline, we have also found from the temperature dependence of the spin-lattice relaxation time that the zero-field splitting does not change drastically when *o*-phenanthroline is added to the sample (Calvo et al.,1982; Calvo, Butler, Isaacson, Okamura, Fredkin and Feher, in preparation). Similarly, an analysis of the temperature dependence of the EPR spectra, to be discussed later, gives a zero-field splitting that is consistent with the values of the parameters given by Eq. 23a for samples with or without added *o*-phenanthroline. To reconcile these findings with those obtained in Butler et al., 1980 we postulate that in the presence of *o*-phenanthroline some RCs lost their iron. If part of the iron that came out were oxidized to high spin ($S = 5/2$) Fe^{3+}, the measured magnetic moment of the sample would increase, accounting for the smaller zero-field slitting reported in Butler et al., 1980.

Since the peak and edges of the spectrum occur at the same g values for RCs with and without *o*-phenanthroline, we used the same D, E/D, $\mathbf{g}_{Fe}$, and $\mathbf{J}$ as before (Eqs. 23a,b,c) to simulate the spectrum. However, in this case the simulated spectrum could not reproduce the increased width, ΔH, of the observed EPR line. In an attempt to broaden the simulated spectrum, we explored the effects of introducing a spread in the values of the spin Hamiltonian parameters. From Table III we see that a change in D, E/D, and J_x changes the splittings of the peak, i.e., introducing a large variance of these parameters would wipe out the characteristic shape of the peak. Consequently, we introduced the following Gaussian spreads in the values of J_y and J_z:

$$J_y = -0.58 \text{ K} \pm 0.14 \text{ K} \tag{24a}$$

$$J_z = -0.58 \text{ K} \pm 0.06 \text{ K} \tag{24b}$$

The simulated spectra now have a plateau region like the experimental spectra rather than two maxima as in the case of the *o*-phenanthroline sample (see Fig. 4 and inset, Fig. 2). The line width ΔH, however, is less for the simulated spectra (460 G) than for the experimental spectra (640 G). In all our attempts to account for the increased line width we varied at most two parameters simultaneously. Perhaps a correlated variation of several parameters would produce a better simulation of the line width without destroying the other characteristics of the line. Although the quantitative agreement between theory and experiment is not as good as for RCs with *o*-phenanthroline, we believe that our theoretical treatment also explains features *a*, *c*, and *d* (given at the end of the Experimental section) for RCs without *o*-phenanthroline.

Frequency Dependence of the Line Width

The observed line width δH is approximately proportional to frequency (Fig. 3). The line width results from the spread of g values due to their dependence on the orientation of the RCs with respect to the magnetic field. We simulated spectra at three frequencies with the spin Hamiltonian parameters of Eqs. 23a,b,c and 24a,b. These calculations produced absorption (χ'') spectra, which we differentiated numerically for comparison with the experimental spectra. The agreement of the observed and calculated line widths, presented in Table IV, confirms that our theoretical treatment explains feature *b*. The dependence of the line width on frequency, for both the observed and calculated spectra, deviates from linearity by ~10% at 9 GHz and by ~15% at 35 GHz. This is caused by the nonlinearity of the Fe^{2+} Zeeman terms (see Fig. 11), which in essence causes the energy denominators E_{ij} in the perturbation expressions for the effective g values to depend on H (see Table IIA).

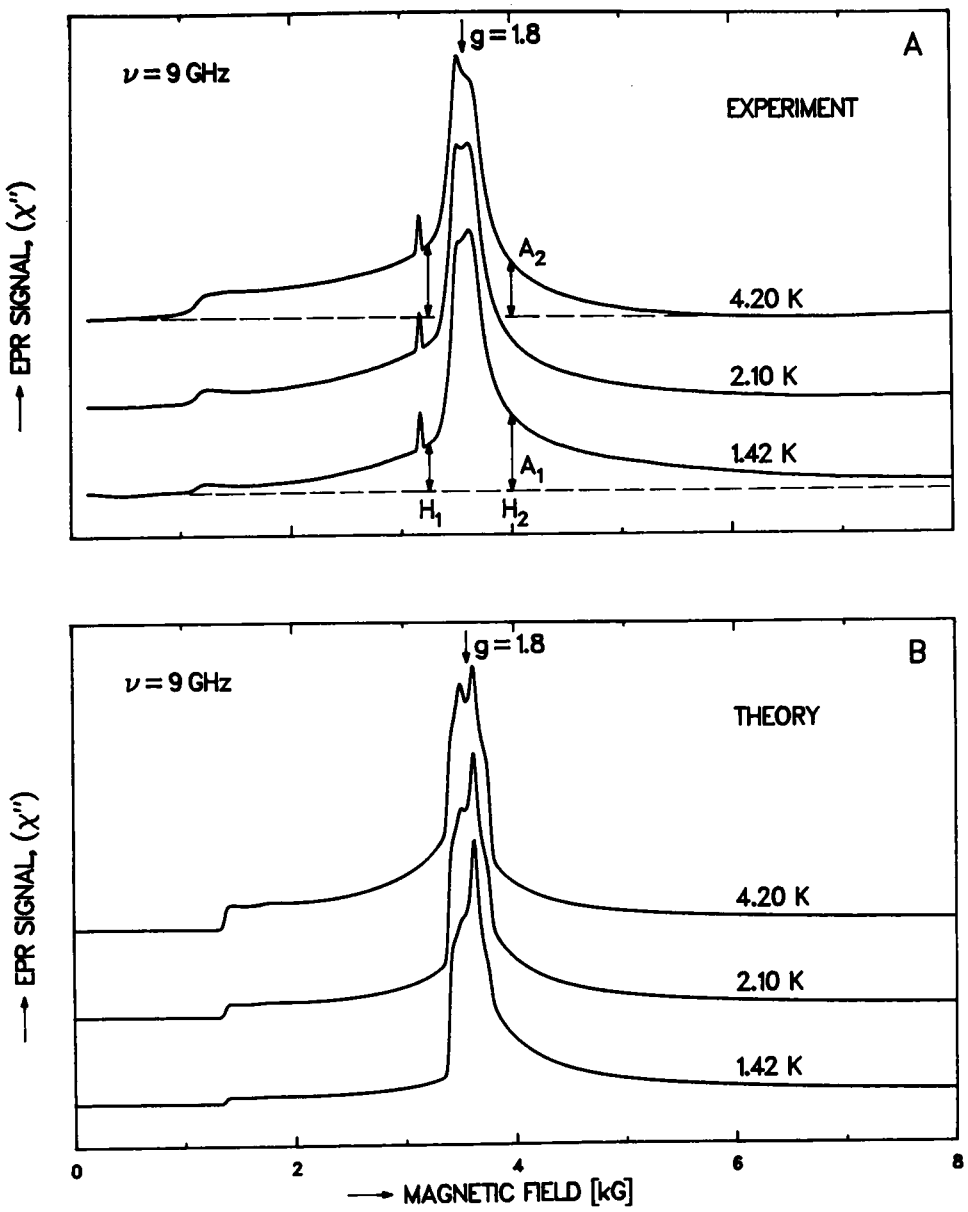

FIGURE 13 Comparison of experimental spectra (*A*) with simulated spectra (*B*). Both (*A*) and (*B*) show that the amplitudes of the two maxima of the peak change with temperature, as does the amplitude of the low-field edge. From the temperature dependence of the amplitudes at H_1 and H_2, the zero-field splitting was independently determined. The amplitudes A_1 and A_2 were used in the decomposition of the observed spectra into the individual contributions of the lowest two doublets (see Fig. 14). Sample was the same as described in the legend of Fig. 2. The spin Hamiltonian parameters used in the simulation are given by Eq. 23.

Temperature Dependence of the Integrated Area

The simulated spectra were integrated from 0 to 8 kG, as described previously for the observed spectra. Using the parameters given by Eqs. 23a,b,c the ratio of the integrated intensities was found to be

$$\text{for } Q_A^-Fe^+: \quad \frac{\int_0^{8\text{ kG}} \chi'' dH \text{ at } 1.40\text{ K}}{\int_0^{8\text{ kG}} \chi'' dH \text{ at } 4.22\text{ K}} = 2.29. \tag{25}$$

TABLE IV
FREQUENCY DEPENDENCE OF EPR LINE WIDTH*

ν	$\delta H_{\text{Experiment}}$	δH_{Theory}
GHz	*G*	*G*
1.18	48 ± 3	45
9.00	330 ± 15	320
35.0	1080 ± 50	1096

*RC sample 1.

This is in agreement with the experimental result of 2.3 ± 0.1 (see Eq. 3 and feature *e*) in the summary of experimental results. The deviation of this value from Curie law (3.01) is due to the reduced area of $\int \chi'' dH$ for $Q^- Fe^{2+}$. The origin of this reduction is the antiferromagnetic interaction between Q^- and Fe^{2+}. This can be seen qualitatively from the following argument: Since 9 GHz (0.43 K) is much less than the Fe^{2+} splittings (>3 K), χ'' is principally due to transitions between the two spin states of the quinone. Although the Kramers-Kronig relation (Abragam and Bleaney, 1970) does not apply rigorously to $\int \chi'' dH$, this quantity should still be approximately proportional to the contribution of the quinone to the static susceptibility χ_0. But in the presence of an antiferromagnetic interaction the quinone contribution to χ_0 is less than for a free spin 1/2 as seen from Fig. 10 in (Butler et al., 1980). Thus $\int \chi'' dH$ will also be less than for a free spin 1/2.

To check the accuracy of integration of the simulated spectra, we evaluated the integrated intensities for $\mathbf{J} = 0$, i.e., a free spin 1/2 not interacting with Fe^{2+}.[13] For this case we calculated

$$\text{for free spin } \tfrac{1}{2}: \quad \frac{\int_0^{8\text{ kG}} \chi'' dH \text{ at } 1.40 \text{ K}}{\int_0^{8\text{ kG}} \chi'' dH \text{ at } 4.22 \text{ K}} = 3.01, \qquad (26)$$

which agrees exactly with the Curie law (4.22/1.40 = 3.01) for a free spin 1/2. The measured ratios of the integrated areas of the spectra of $Q_A^- Fe^{2+}$ and D^+ obtained by light modulation (Eq. 5) cannot be compared directly with theory[14] because of the relaxation effect discussed in the section following Eq. 5.

Low-field Edge of the Spectrum

Our theory predicts a low-field edge in the spectrum as is indeed observed experimentally. There is, however, a difference in the exact position of the low-field edge between the observed and simulated spectra. In the simulated spectra the edge always has a smaller *g* value (larger magnetic field) than in the observed spectra. We recall that in a frozen sample only those RCs whose *y*-axes are aligned nearly along the applied magnetic field contribute to the EPR signal at the edge $g_{2,y}$ (Fig. 9). This may be the reason why the approximate spin Hamiltonian (Eq. 11) accounts less well for the edge position than for the other features. Averaging over the many orientations of RCs with the *y*-axis not aligned near the field makes the approximate nature of the Hamiltonian less noticeable than at the edges where only a few orientations are averaged.

Decomposition of the Observed EPR Spectra into the Individual Contributions of the Lowest Two Doublets

Since the EPR spectra are composed of two contributions, arising from the ground doublet and the first excited doublet, one should be able to separate the individual contributions experimentally. This was accomplished by subtracting spectra obtained at two temperatures after first normalizing them at either high or low fields where only one doublet contributes to either spectrum (see Fig. 12). For the high-field position (where only the ground doublet is expected to contribute) we chose a value of 4 kG. The ratio of amplitudes at 1.4 and 4.2 K, A_1/A_2, (see Fig. 13 *A*) at this field was determined to be 1.37. After multiplying the 4.2 K spectrum by this value and subtracting the 1.4 K spectrum from it, we obtained the spectrum of the excited doublet as shown in Fig. 14 *A*. An analogous procedure was followed at 3.25 kG to obtain the spectrum of the ground doublet. The intensities of the two "difference" spectra were adjusted to have the same maximum value. Small negative intensities observed in the high- and low-field wings of the difference spectra (excited and ground doublets, respectively) were deleted. They presumably were due to baseline drifts that introduced an error in the integration of the field modulation spectra.

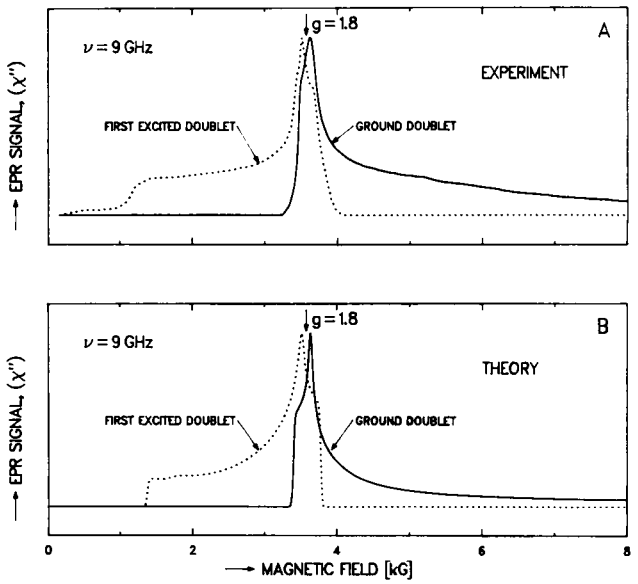

FIGURE 14 Comparison of the experimentally deduced spectra of the ground and excited doublet (*A*) with theory (*B*). The observed spectra of Fig. 13 *A* were decomposed as described in the text. The spin Hamiltonian parameters used for the simulations of (*B*) are given by Eq. 23. The good agreement between experiment *A* and theory *B* provides strong evidence of the essential validity of our theoretical model.

[13]Because the simulations produce delta function spectra, we introduced an artificial width by making $g_{Q,x}$ and $g_{Q,z}$ deviate from $g_{Q,y}$ by ±0.005, respectively. (The theoretical result was the same for *g* anisotropies of 0.01 and 0.05.)

[14]Integration of the theoretical spectra gives a ratio of 0.87 at 4.22 K and 0.66 at 1.40 K.

Simulations of the individual spectra of each doublet using the parameters given by Eqs. 23a,b,c are shown in Fig. 14 *B*. They are remarkably similar in appearance to the experimentally determined difference spectra. A quantitative comparison of the two sets of spectra shows that the peak positions agree within ±20 G, the edges ($H_{i,z}$ in Fig. 12) within ±50 G, and the relative intensities throughout most of the spectrum within ±20%.

Determination of Zero-field Splitting from the Temperature Dependence of the Spectra

The spin Hamiltonian parameters D and E/D used in the simulations (Eq. 23a) give $E_{21} = 3.2 \pm 0.3$ K (Appendix B of Butler et al., 1980) for the zero-field splitting between the ground doublet and first excited doublet. We analyzed the temperature dependence of the observed spectra in Fig. 13 *A* to determine what splitting we could infer from them. For magnetic fields H_2 greater than the field at $H_{2,z}$ we expect contributions to the spectra only from the ground doublet (see Fig. 12); for fields H_1 less than that at $H_{1,z}$ we expect contributions only from the first excited doublet. The ratio of the amplitudes at these two fields (see Fig. 13 *A*) should vary with temperature according to the Boltzmann factor

$$A(H_1)/A(H_2) = \text{constant} \cdot e^{-E_{21}/k_B T}. \qquad (27)$$

A logarithmic plot of the amplitude ratios vs. reciprocal temperature for sample No. 2 gave a straight line whose slope was $-E_{21}/k_B$. For $H_2 = 4.5$ kG and $H_1 = 3.0$ kG, we obtained $E_{21} = 3.3 \pm 0.3$ K, in agreement with the value obtained from the magnetization measurements (Butler et al., 1980, Appendix B). Other combinations of H_1 and H_2 gave similar results. We conclude that the temperature dependence of the observed spectra is explained well by our theory and is consistent with the zero-field splitting predicted by the values of the spin Hamiltonian parameters D and E/D of Eq. 23a.

Preferential Variation of the High-field Part of the EPR Line with Environmental Conditions

We noted (end of experimental section, feature *g*) that for $Q_A^- Fe^{2+}$ in different environments, the variations in line width δH are principally due to changes in g_2 (see Fig. 1 *B* and Table I). From Table I, the variations in g_2 are an order of magnitude greater than those of g_1 (the means and standard deviations are $g_1 = 1.839 \pm 0.001$ and $g_2 = 1.714 \pm 0.012$). Our sensitivity calculations (Table III) showed that D, E/D, and J_z are the parameters that principally affect g_2. They also showed that D and E/D cannot vary too much without changing the maxima splitting or the peak location at $g = 1.8$. Thus we infer from the larger changes in g_2 that, in terms of our model, J_z is more sensitive to the environment than the other spin Hamiltonian parameters.

SUMMARY AND DISCUSSION

We have investigated the EPR spectra of the $Q^- Fe^{2+}$ complex in RCs and have developed a theoretical model that explains the salient features of the observed spectra. In this model, the Fe^{2+} resides in an asymmetric crystalline field that splits the degenerate Fe^{2+} ($S = 2$) ground manifold into five levels. Each level is converted by the spin on Q^- into a doublet. The first excited doublet is sufficiently low in energy to be thermally populated at liquid helium temperature. The observed spectrum is, therefore, a superposition of the spectra of the two lowest lying doublets weighted by the appropriate Boltzmann factor. An external magnetic field imparts to each Fe^{2+} level an anisotropic magnetic moment that couples antiferromagnetically to the spin on Q^-. It is this anisotropy that gives rise to the large line width observed in unoriented samples.

We described the above model with a spin Hamiltonian (Eq. 11) making the simplifying assumptions that the **J** (magnetic interaction) and $\mathbf{g}_{Fe}$ tensors are diagonal and collinear (i.e., have the same principal axes as the crystalline field). We numerically calculated the EPR spectrum from the Hamiltonian, using the values of D, E/D, and $\mathbf{g}_{Fe}$ derived from magnetization data (Butler et al., 1980) and searching for a **J** to optimize the agreement of the simulated spectrum with the observed one. Good agreement was obtained for the position of the peak, the splitting of the peak (Fig. 13), the general line shape, and the frequency (Table IV) and temperature dependence of the spectrum. Poorer agreement was obtained for the position of the low-field edge of the line and the line width of the sample that did not contain *o*-phenanthroline. The EPR line from the third doublet was not observed (see Discussion below). We conclude that our model is basically correct and that its deficiencies are not severe, considering the complexity of the system. We believe that further improvements could have been obtained by a more complicated model, e.g., higher-order crystalline field terms, incorporating nondiagonal magnetic interactions, lifting the requirements of collinearity of **J** and $\mathbf{g}_{Fe}$ with the crystal field tensor, and introducing correlated variances to explain the line widths. However, we did not feel that such further improvements would sufficiently enhance our understanding of the structure to justify the large computational effort involved. We shall now discuss some of the findings and their implications in more detail.

All the observed spectra could be accounted for by the contributions of the two lowest doublets, with no contributions from the remaining three doublets. In simulations at high temperatures (>20 K), the fourth and fifth doublets contribute similar spectra to those from the first and second doublets. However, the third doublet is predicted to be about 15 K above the ground doublet. Furthermore, the

simulations predict a narrow EPR line near $g = 2$, due to this doublet, to appear above ~8 K. We did not observe such an additional peak at higher temperatures (Fig. 5). There are several possible explanations to account for this. The third doublet may have been broadened by a fast relaxation time and its contribution to the observed line could, therefore, have been reduced. It is also possible that the spin Hamiltonian may accurately model the splitting of the lowest two doublets while underestimating the splitting to the third doublet (this could be the case if a second manifold of Fe^{2+} states is not sufficiently far removed from the ground quintet). A large splitting to this doublet would have little effect on the magnetization results of Butler et al., 1980, which is currently the only other experimental check of the validity of the Hamiltonian. EPR spectra from oriented samples (e.g., crystals) should give narrower lines to help resolve this question.

The difference in line width between the EPR spectra obtained in the presence and absence of *o*-phenanthroline (Fig. 2) indicates that a structural change occurs when *o*-phenanthroline is bound. *o*-phenanthroline is an inhibitor of electron transfer from Q_A to Q_B (Parson and Case, 1970; Clayton et al., 1972), but there is evidence that it does not chelate Fe in RCs (Butler et al., 1980; Eisenberger et al., 1982; Bunker et al., 1982; Boso, et al., 1981*b*). The fact that binding of *o*-phenanthroline changed the line width without changing the g value suggests that the average values of the spin Hamiltonian parameters have not been significantly changed. However, their variance in the absence of *o*-phenanthroline may have been increased, indicating a greater structural variability in the region around the Q^-Fe^{2+} complex. Binding *o*-phenanthroline could result in "locking in" certain structures of the protein, thus limiting the variations in the spin Hamiltonian parameters. The observation that the line width for RCs with *o*-phenanthroline is approximately the same as for chromatophores (Table I) suggests that the environment of Fe^{2+} in both systems is similar.

The magnetic interaction **J** (Eq. 23c) can be separated into isotropic, $\mathbf{J}_I$ and anisotropic, $\mathbf{J}_A$ terms, i.e.,

$$\mathbf{J} = \mathbf{J}_I + \mathbf{J}_A, \tag{28}$$

with $J_I = -0.43$ K, $J_{A,x} = +0.30$ K, $J_{A,y} = -0.15$ K, and $J_{A,z} = -0.15$ K. Coffman and Buettner (1979) reviewed many experimental determinations of isotropic superexchange interactions in well-characterized systems. From these data they deduced a limit function relating the maximum distance between two spins to a given long range superexchange interaction, J, between the spins. Using our value of J_I, we obtain from their limit function an iron-quinone distance <10 Å. Unfortunately, all the compounds in their survey were metal dimers, casting some doubt on the applicability of their results to the iron-quinone complex. Recently, complexes with two *o*-semiquinones liganded directly to iron have been reported, but J was not determined and the iron was Fe^{3+} (Lynch et al., 1982); however, a program was outlined that may yield a high-spin Fe^{2+} complex with two *p*-semiquinones (singly reduced ubiquinone in RCs is *p*-semiquinone) attached to the ligand framework. Characterization of such a model compound would be a great aid in understanding the iron-quinone complex in RCs.

The anisotropic term $\mathbf{J}_A$ can arise from either anisotropic superexchange, dipole-dipole interaction or a combination of both. $\mathbf{J}_A$ has the form of a purely dipolar interaction with the interacting species both lying on the x axis. If we assume that $\mathbf{J}_A$ is entirely dipolar, using a point-dipole model we deduce an iron-quinone distance of 2.6 Å. EXAFS measurements on Fe^{2+} in RCs (Eisenberger et al., 1982) showed that the average first coordination shell ligand distance is 2.10 ± 0.02 Å, with a more distant shell at 4.14 ± 0.05 Å (assigned to the third or higher shell). The EXAFS results indicated that Q_B is not in the first coordination shell; furthermore, magnetization results (Butler et al., 1980) and Mossbauer results (Boso et al., 1981*a,b*) indicated that neither Q_A nor Q_B is in the first coordination shell. An iron-quinone distance of 2.6 Å is certainly outside the first coordination shell, in agreement with the previous results, but it is probably too small for the second coordination shell (the second shell was not observed in the EXAFS measurements [Eisenberger et al., 1982]).

If, in addition to a dipolar interaction, we consider an anisotropic superexchange contribution to $\mathbf{J}_A$, the calculated iron-quinone distance will be >2.6 Å (the anisotropic superexchange is expected to be antiferromagnetic, since ferromagnetic superexchange is rare and requires a special geometry [Martin, 1968]). Without detailed structural information for the iron-quinone complex, nothing more can be deduced concerning possible anisotropic superexchange.

For simplicity, we assumed that **J** and $\mathbf{g}_{Fe}$ are diagonal tensor interactions which are collinear with the crystal-field principal axes. In general this would not be expected for **J**; the general tensor interaction would have nine independent parameters. Searching with so many adjustable parameters for a best simulation of the EPR spectrum would be prohibitive without additional experimental information, such as might be obtained from EPR spectra of single crystals of RCs (see below). We did calculate spectra for nondiagonal **J**'s that were obtained by small angle rotations (<15°) of **J** (Eq. 23c). These calculations showed that the simulated spectra are not highly sensitive to the principal axes of **J**. On the other hand, the assumed tensor form of $\mathbf{g}_{Fe}$ is well-founded theoretically (Butler et al., 1980, Appendix A). Variations in $\mathbf{g}_{Fe}$ have little effect on the simulated spectrum as long as the rms g value does not change. We did find, however, that the values of $\mathbf{g}_{Fe}$ given by Eq. 23b produced a better fit to the magnetization data (Butler et al., 1980, Fig. 10) than did an isotropic g

value, when used with the D, E/D, and $\mathbf{J}$ of Eqs. 23a,c. The calculated and observed magnetization agreed within the error bars.

From the microwave saturation experiments we have found that the spin-lattice relaxation time T_1 in $Fe^{2+}Q_B^-$ was ~40% shorter than in $Q_A^-Fe^{2+}$. If we assume that the relaxation time is governed by the Fe^{2+} coupled via a dipolar interaction to the quinone spin, the relative distances, r_A and r_B, of Q_A and Q_B from Fe^{2+}, are given by (e.g., Norris et al., 1980)

$$\frac{r_A}{r_B} = \left[\frac{T_1(Q_A^-Fe^{2+})}{T_1(Fe^{2+}Q_B^-)}\right]^{1/6} = (1.4)^{1/6} = 1.06. \quad (29)$$

If, on the other hand, the coupling is via an exchange interaction involving orbital overlaps, one expects T_1 to be proportional to $(e^{r/r_0})^2$, where r_0 is some reference length for orbital overlap. In this case

$$\frac{r_A - r_B}{r_0} = \tfrac{1}{2}\ln(1.4) = 0.17. \quad (30)$$

Thus both Eq. 29 and Eq. 30 predict that Q_A and Q_B are approximately equidistant from the Fe^{2+}. This conclusion is also consistent with the similarity of the observed spectra of $Q_A^-Fe^{2+}$ and $Fe^{2+}Q_B^-$ (Fig. 6).

The EPR data presented in this paper were obtained from frozen solutions of RCs. The observed EPR signal is, therefore, a superposition of EPR signals originating from RCs randomly oriented with respect to the applied magnetic field. To obtain values of the parameters of the magnetic interaction from these data required a complicated numerical averaging of the spectra. A great deal of information is lost in this process. A sample with oriented RCs (e.g., crystals) would obviate this problem.

Single crystals of RCs from *Rhodopseudomonas viridis* (Michel, 1982) and *R. sphaeroides* R-26 (Allen and Feher, 1983; Feher and Okamura, 1983; Allen and Feher, 1984) have recently been obtained. EPR measurements on these crystals should provide several advantages. The narrower EPR lines of the Q^-Fe^{2+} complex should make it possible to observe signals from the higher excited doublets. A detailed study of the angular dependence of the EPR signal with respect to the external magnetic field should allow a better check of the spin Hamiltonian and a more accurate determination of its parameters, in particular the value of $\mathbf{J}$ and its principal axes with respect to the crystal field axes.

In conclusion, we have described a spin Hamiltonian model of the quinone-iron acceptor complex in RCs that satisfactorily accounts for the observed static magnetization and EPR spectrum of this complex. From this model we have determined that Fe^{2+} resides in an asymmetric ligand field environment and that it interacts with Q^- in reduced RCs through an anisotropic tensor magnetic interaction. From the value of this tensor we have deduced limitations on the Q^-Fe^{2+} separation, for both primary and secondary quinones. Further structural information must depend on other experimental techniques, particularly EPR and x-ray diffraction of single crystals.

APPENDIX A

Perturbation Calculation of the Principal g Values for the Two Lowest Doublets

We divide the spin Hamiltonian (Eq. 11) into a zeroth-order Hamiltonian

$$\mathcal{H}_0 = D[(S_{Fe,z}^2 - \tfrac{1}{3}S_{Fe}(S_{Fe}+1)) + (E/D)(S_{Fe,x}^2 - S_{Fe,y}^2)] \quad (A1)$$

and a perturbation

$$\mathcal{H}' = \mu_B\mathbf{H}\cdot\mathbf{g}_{Fe}\cdot\mathbf{S}_{Fe} + g_Q\mu_B\mathbf{H}\cdot\mathbf{S}_Q - \mathbf{S}_{Fe}\cdot\mathbf{J}\cdot\mathbf{S}_Q. \quad (A2)$$

The eigenvalues of $\mathcal{H}_0$ are E_i ($i = 1,\ldots,5$, $E_1 < E_2 < \ldots$), with corresponding eigenvectors $|i\rangle|Q\rangle$, where $|i\rangle$ is the Fe^{2+} state and $|Q\rangle$ is any vector in the two-dimensional ($S_Q = 1/2$) spin state space of Q^-. When we apply degenerate perturbation theory to the ith doublet, we obtain an effective Hamiltonian $\mathcal{H}_i$ (Eq. 21), from which we obtain an effective g tensor $\mathbf{g}_i$. We know from the elementary discussion that we must compute $\mathbf{g}_i$ to at least order J^2 to obtain the main features of the observed EPR signal, so we must compute $\mathcal{H}_i$ to third order. Define

$$G_i = \sum_{j\neq i}\frac{|j\rangle\langle j|}{E_j - E_i}. \quad (A3)$$

Then the standard expression for $\mathcal{H}_i$ is (Schiff, 1968)

$$\begin{aligned}\mathcal{H}_i = E_i &+ \langle i|\mathcal{H}'|i\rangle - \langle i|\mathcal{H}'G_i\mathcal{H}'|i\rangle \\ &+ \langle i|\mathcal{H}'G_i\mathcal{H}'G_i\mathcal{H}'|i\rangle \\ &- \tfrac{1}{2}\langle i|\mathcal{H}'G_i^2\mathcal{H}'|i\rangle\langle i|\mathcal{H}'|i\rangle \\ &- \tfrac{1}{2}\langle i|\mathcal{H}'|i\rangle\langle i|\mathcal{H}'G_i^2\mathcal{H}'|i\rangle. \end{aligned} \quad (A4)$$

Note that $\langle i|\ldots|i\rangle$ are 2×2 matrices in the spin space of Q^-, and matrix multiplication is implied.

The first-order result is

$$\mathcal{H}_i^{(1)} = g_Q\mu_B\mathbf{H}\cdot\mathbf{S}_Q, \quad (A5)$$

from which the zero-order g tensor is just

$$g_i^{(0)} = g_Q. \quad (A6)$$

The second-order result is

$$\mathcal{H}_i^{(2)} = \mathcal{H}_i^{(HH)} + \mathcal{H}_i^{(JJ)} + \mathcal{H}_i^{(HJ)}, \quad (A7)$$

where

$$\mathcal{H}_i^{(HH)} = -\sum_{\nu=xyz}\langle i|S_{Fe,\nu}G_iS_{Fe,\nu}|i\rangle g_{Fe,\nu}^2\mu_B^2H_\nu^2 \quad (A8)$$

is the second-order level shift due to the magnetic field acting on Fe^{2+},

$$\mathcal{H}_i^{(JJ)} = -\frac{1}{4}\sum_{\nu=xyz}\langle i|S_{Fe,\nu}G_iS_{Fe,\nu}|i\rangle J_\nu^2 \quad (A9)$$

is the second-order level shift due to the magnetic interaction (both $\mathcal{H}_i^{(HH)}$

and $\mathcal{H}_i^{(HJ)}$ are independent of the Q^- spin), and

$$\mathcal{H}_i^{(HJ)} = 2 \sum_{\nu=xyz} \langle i | S_{\mathrm{Fe},\nu} G_i S_{\mathrm{Fe},\nu} | i \rangle J_\nu g_{\mathrm{Fe},\nu} \mu_B H_\nu S_{Q,\nu}, \quad \text{(A10)}$$

which gives a first-order g shift

$$\delta g_{i,\nu}^{(1)} = 2 \langle i | S_{\mathrm{Fe},\nu} G_i S_{\mathrm{Fe},\nu} | i \rangle J_\nu g_{\mathrm{Fe},\nu}. \quad \text{(A11)}$$

This g shift is associated with the effective magnetic field seen by the Q^- spin, as in the elementary treatment. From $\mathcal{H}_i^{(HH)}$ we obtain the Fe^{2+} magnetic polarizability

$$\alpha_{i,\nu} = -\frac{\partial^2 \mathcal{H}_i^{(HH)}}{\partial H_\nu^2} = 2 \langle i | S_{\mathrm{Fe},\nu} G_i S_{\mathrm{Fe},\nu} | i \rangle g_{\mathrm{Fe},\nu}^2 \mu_B^2. \quad \text{(A12)}$$

Recalling the relation $m_{\mathrm{Fe},\nu} = -g_{\mathrm{Fe},\nu}\mu_B S_{\mathrm{Fe},\nu}$ between magnetic moment and spin, the magnetic interaction energy can be written

$$-\sum_{\nu=xyz} J_\nu S_{\mathrm{Fe},\nu} S_{Q,\nu} = \sum_{\nu=xyz} \frac{J_\nu}{g_{\mathrm{Fe},\nu} g_Q \mu_B^2} m_{\mathrm{Fe},\nu} g_Q \mu_B S_{Q,\nu}$$

$$= \sum_{\nu=xyz} \lambda_\nu m_{\mathrm{Fe},\nu} g_Q \mu_B S_{Q,\nu}. \quad \text{(A13)}$$

Consequently, the Q^- spin sees the magnetic interaction field $\Sigma_{\nu=xyz} \lambda_\nu m_{\mathrm{Fe},\nu} = \Sigma_{\nu=xyz} \alpha_{i,\nu} H_\nu$ and as in the elementary treatment, there is a g shift

$$\delta g_{i,\nu}^{(1)} = g_Q \lambda_\nu \alpha_{i,\nu} = g_Q \frac{2 J_\nu}{g_{\mathrm{Fe},\nu} g_Q \mu_B^2} \langle i | S_{\mathrm{Fe},\nu} G_i S_{\mathrm{Fe},\nu} | i \rangle g_{\mathrm{Fe},\nu}^2 \mu_B^2, \quad \text{(A14)}$$

which is the same as Eq. A11.

The third-order result is

$$\mathcal{H}_i^{(3)} = \mathcal{H}_i^{(JJJ)} + \mathcal{H}_i^{(JJHa)} + \mathcal{H}_i^{(JJHb)} \quad \text{(A15)}$$

where $\mathcal{H}^{(JJJ)} \propto J_x J_y J_z$ is the third-order analogue of $\mathcal{H}_i^{(JJ)}$ (consequently, it is independent of the magnetic field and of the Q^- spin),

$$\mathcal{H}_i^{(JJHa)} = -\frac{1}{2} \sum_{\substack{\nu,\sigma=xyz \\ \nu \neq \sigma}} \langle i | S_{\mathrm{Fe},\sigma} G_i^2 S_{\mathrm{Fe},\sigma} | i \rangle J_\sigma^2 g_Q \mu_B H_\nu S_{Q,\nu}, \quad \text{(A16)}$$

and $\mathcal{H}_i^{(JJHb)}$ will be defined later. The origin of $\mathcal{H}_i^{(JJHa)}$ is the first-order Zeeman shift ($\mathcal{H}_i^{(1)}$) of the energy denominators (hidden in the symbol G_i) in $\mathcal{H}_i^{(JJ)}$, which produces the second-order magnetic interaction shift in the Fe^{2+} energy levels. This term was explained in the elementary discussion, although we limited ourselves to the lowest two Fe^{2+} levels. The corresponding second order g shifts are

$$\delta g_{i,\nu}^{(2a)} = -\frac{g_Q}{2} \sum_{\substack{\sigma=xyz \\ \sigma \neq \nu}} \langle i | S_{\mathrm{Fe},\sigma} G_i^2 S_{\mathrm{Fe},\sigma} | i \rangle J_\sigma^2. \quad \text{(A17)}$$

We do not have a simple explanation for the remaining third-order term in the effective Hamiltonian, $\mathcal{H}_i^{(JJHb)}$, so we just present it

$$\mathcal{H}_i^{(JJHb)} = \sum_{\nu=xyz} g_{i,\nu}^{(2b)} \mu_B H_\nu S_{Q,\nu}, \quad \text{(A18)}$$

where the g values are given by

$$\delta g_{i,x}^{(2b)} = i g_{\mathrm{Fe},x} J_y J_z [\langle i | S_{\mathrm{Fe},x} G_i S_{\mathrm{Fe},y} G_i S_{\mathrm{Fe},z} | i \rangle$$
$$+ \langle i | S_{\mathrm{Fe},y} G_i S_{\mathrm{Fe},z} G_i S_{\mathrm{Fe},x} | i \rangle$$
$$- \langle i | S_{\mathrm{Fe},z} G_i S_{\mathrm{Fe},x} G_i S_{\mathrm{Fe},y} | i \rangle]; \quad \text{(A19)}$$

$\delta g_{i,y}^{(2b)}$ and $\delta g_{i,z}^{(2b)}$ are obtained by cyclic permutation of x, y, z. The numbers $\delta g_{i,\nu}^{(2b)}$ are real.

The matrix elements that appear in the g shifts are expressed in terms of the Fe^{2+} spin Hamiltonian parameters D and E in Table IIB. The g shifts are presented in Table IIA.

APPENDIX B

Numerical Calculation of the EPR Spectrum

Resonance Field. In this appendix we describe the numerical calculation of the EPR spectrum from the spin Hamiltonian $\mathcal{H}$ (Eq. 11). For a given set of parameters D, E, $\mathbf{g}_{\mathrm{Fe}}$, g_Q, and $\mathbf{J}$, and for the applied magnetic field in the direction $\hat{\mathbf{n}}$, the energy levels of $\mathcal{H}$ are the eigenvalues of its matrix representation. These energy eigenvalues are determined numerically as described in Butler et al., 1980. The 10 energy levels occur in pairs as Kramers doublets (labeled $i = 1, \ldots, 5$), which are degenerate at zero applied magnetic field. At magnetic field H, $\delta E_i(H, \hat{\mathbf{n}})$ is the difference in energy between the two levels $i\downarrow$ and $i\uparrow$ of the ith doublet.[15] For any frequency ν, there is at least one resonance field $H_i(\hat{\mathbf{n}})$ for which $\delta E_i(H_i, \hat{\mathbf{n}}) = h\nu$. If there is more than one resonance field for a given ν and $\hat{\mathbf{n}}$, only the smallest is considered. The resonance field $H_i(\hat{\mathbf{n}})$ is found iteratively. Initially we calculated $\delta E_i - h\nu$ for two values of the magnetic field. The next point of the iteration was found by a linear interpolation/extrapolation using Aitken's algorithm (Dahlquist et al., 1974). The iterative solution was continued by quadratic interpolation/extrapolation using Aitken's algorithm, until $\delta E_i - h\nu$ is zero within a specified tolerance. The resonance fields $H_i(\hat{\mathbf{n}})$ are calculated on a discrete set of $\hat{\mathbf{n}}$ within the principal octant of directions (i.e., $n_x > 0$, $n_y > 0$, $n_z > 0$), which by symmetry suffices for all directions (Butler et al., 1980).

Resonance Intensity. The relative intensity of the EPR line spectrum for each $H_i(\hat{\mathbf{n}})$ is obtained by calculating the relative power absorbed from the microwave field. In this calculation we consider only the line spectrum due to a sharp EPR transition (i.e., no natural line width).

The Hamiltonian for the interaction between the Q^-Fe^{2+} complex and the microwave radiation field is given by

$$\mathcal{H}_{\mathrm{Int}} = \mu_B \mathbf{H}_1(t) \cdot \mathbf{g}_{\mathrm{Fe}} \cdot \mathbf{S}_{\mathrm{Fe}} + g_Q \mu_B \mathbf{H}_1(t) \cdot \mathbf{S}_Q, \quad \text{(B1)}$$

where $\mathbf{H}_1(t)$ is the microwave radiation field

$$\mathbf{H}_1(t) = \mathbf{H}_1 \cos(2\pi\nu t). \quad \text{(B2)}$$

The radiation field is always perpendicular to the static field direction, but this still leaves the direction arbitrary within the plane perpendicular to $\hat{\mathbf{n}}$. We specify this arbitrary orientation by the angle ψ measured from the x'-axis in the primed coordinate system obtained by standard Euler rotations through angles ϕ about the original z-axis and θ about the intermediate y-axis (θ and ϕ are the polar coordinates of $\hat{\mathbf{n}}$). As explained in Butler et al., 1980, $0 \leq \psi \leq \pi/2$ covers all possibilities because of the requirement for time reversal invariance for $\mathcal{H}_{\mathrm{Int}}$. Letting $\hat{\mathbf{x}}'$ and $\hat{\mathbf{y}}'$ be unit vectors of the primed coordinate system axes, the interaction Hamiltonian can be written as

$$\mathcal{H}_{\mathrm{Int}} = \mu_B H_1 \cos(2\pi\nu t)[(\cos\psi \hat{\mathbf{x}}' + \sin\psi \hat{\mathbf{y}}') \cdot \mathbf{S}_T], \quad \text{(B3)}$$

where

$$\mathbf{S}_T = \mathbf{g}_{\mathrm{Fe}} \cdot \mathbf{S}_{\mathrm{Fe}} + g_Q \mathbf{S}_Q. \quad \text{(B4)}$$

[15] For simplicity, we label the two states of each doublet $\downarrow$ and $\uparrow$, although there is some mixing of these pure states.

The power absorbed from the microwave field (per Q^-Fe^{2+} complex) is the product of the microwave energy, $h\nu$, and the transition probability per unit time, w, for the interaction, weighted by a Boltzmann factor for the population difference of the two states involved in the transition. This is true only if the microwave power is sufficiently small, so that the transition is not saturated; this condition was maintained during the experiments.

We used time-dependent perturbation theory (Schiff, 1968) to calculate the transition rate $w_{i\uparrow,i\downarrow}$ induced by $\mathcal{H}_{\text{Int}}$, where $|i\downarrow\rangle$ and $|i\uparrow\rangle$ are the two states of the ith doublet at the resonance field $H_i(\hat{\mathbf{n}})$. From Fermi's golden rule applied to a periodic perturbation like Eq. B3, the result is

$$w_{i\uparrow,i\downarrow} = \frac{\pi^2}{h} |\langle i\uparrow | \mathcal{H}_{\text{Int}} | i\downarrow \rangle|^2 \delta(E_{i\uparrow} - E_{i\downarrow} - h\nu). \tag{B5}$$

Because the RCs are randomly oriented, we must average over the possible values of ψ, which gives

$$|\langle i\uparrow | \mathcal{H}_{\text{Int}} | i\downarrow \rangle|^2 = \tfrac{1}{2}(\mu_B H_1)^2 M^2_{i\uparrow,i\downarrow} \tag{B6a}$$

where

$$M_{i\uparrow,i\downarrow} = \tfrac{1}{2}(\mu_B H_1)^2 [|\langle i\uparrow | \hat{x}' \cdot \mathbf{S}_T | i\downarrow \rangle|^2 + |\langle i\uparrow | \hat{y}' \cdot \mathbf{S}_T | i\downarrow \rangle|^2]. \tag{B6b}$$

The power absorbed per RC per unit microwave power is then

$$P_i = \left(\frac{h\nu w_{i\uparrow,i\downarrow}}{H_1^2}\right)(1 - e^{-h\nu/k_BT}) \left[\frac{e^{-E_{i\downarrow}/k_BT}}{\sum_{k=1}^{10} e^{-E_k/k_BT}}\right]$$

$$= \frac{\pi^2}{2} \nu \mu_B^2 M^2_{i\uparrow,i\downarrow} \delta(E_{i\uparrow} - E_{i\downarrow} - h\nu) (1 - e^{-h\nu/k_BT}) \left[\frac{e^{-E_{i\downarrow}/k_BT}}{\sum_{k=1}^{10} e^{-E_k/k_BT}}\right]. \tag{B7}$$

We now have calculated the resonance field $H_i(\hat{\mathbf{n}})$ and the relative power absorbed, $P_i(\hat{\mathbf{n}})$, for the static magnetic field in the direction $\hat{\mathbf{n}}$. To determine the EPR spectrum for a sample of randomly oriented RCs, we must average over all directions $\hat{\mathbf{n}}$. We want to calculate $\mathcal{I}(H)$, the intensity of the EPR spectrum as a function of the applied magnetic field H. To do this we must first convert the delta function of energy in Eq. B7 to a delta function of magnetic field. The result is

$$\delta(E_{i\uparrow} - E_{i\downarrow} - h\nu) = \frac{1}{\left|\frac{\partial (E_{i\uparrow} - E_{i\downarrow})}{\partial H}\right|} \delta[H - H_i(\hat{n})]$$

$$= \frac{1}{|\mu_{i\uparrow} - \mu_{i\downarrow}|} \delta[H - H_i(\hat{n})] \tag{B8}$$

where $\mu_{i\downarrow}$ is the magnetization of the $i\downarrow$ level. The expression for the intensity of the EPR spectrum is now obtained by averaging over all directions $\hat{\mathbf{n}}$ of the principal octant of the polar coordinate system

$$\mathcal{I}(H) = \frac{2}{\pi} \int_0^{\pi/2} \sin\theta \, d\theta \int_0^{\pi/2} d\phi \, I_i(\hat{n}) \delta[H - H_i(\hat{n})] \tag{B9}$$

where

$$I_i(\hat{n}) = \frac{P_i(\hat{n})}{|\mu_{i\uparrow} - \mu_{i\downarrow}|}. \tag{B10}$$

An alternative treatment of the simulation of powder line shapes, emphasizing the difference between field-swept and frequency-swept spectrometers is given by Aasa and Vanngard (1975). They obtained the same correction as Eq. B10 and pointed out that many previous treatments have introduced significant errors by overlooking it. The numerical methods used to evaluate Eq. B9 are presented in the following section.

Numerical Techniques. The evaluation of the surface integral in Eq. B9 is straightforward. The effect of the delta function is to convert the surface integral into a line integral along a path in the principal octant. This path is selected by satisfying the delta function condition, thus picking out a path $l(\theta, \phi)$ such that

$$H_i(\theta, \phi) = H \tag{B11}$$

where H is the applied magnetic field. Effectively, this selects the contours of H_i and integrates the intensity $I_i(\theta, \phi)$ along the contour. To simplify the integration, the change of variables $\theta \rightarrow u = \cos\theta$ was performed. Then, by defining a path length parameter l, the contour path satisfies the pair of differential equations

$$\frac{du}{dl} = \mp \frac{\partial H_i(u, \phi)}{\partial \phi} \tag{B12}$$

$$\frac{d\phi}{dl} = \pm \frac{\partial H_i(u, \phi)}{\partial u} \tag{B13}$$

and the integral $\mathcal{I}(H)$ satisfies the differential equation

$$\frac{d\mathcal{I}}{dl} = I_i(u, \phi). \tag{B14}$$

By solving the system of three equations B12, B13, and B14, the path l and the integral $\mathcal{I}(H)$ along the path are simultaneously evaluated. The initial conditions for $l = 0$ are found by picking a pair u and ϕ along one of the edges of the principal octant where $H_i(u, \phi)$ has the desired value H and setting $\mathcal{I}(H) = 0$. The sign ambiguity in Eqs. B12 and B13 is resolved by picking the sign that provides integration into the octant from the initial point. The integration is terminated when $u(l)$, $\phi(l)$ again reach a boundary of the octant, at which point the value of the integral of Eq. B14 is $\mathcal{I}(H)$. The numerical integration of this system of equations was carried out by using the Adams-Moulton method of subroutine DGEAR from the IMSL library.

The evaluation of $H_i(\hat{\mathbf{n}})$ and $I_i(\hat{\mathbf{n}})$ by the iterative procedure is rather time consuming, so only a relatively small number of points in the principal octant could be evaluated (typically ~40 points). The integration of Eqs. B12–B14, however, requires knowledge of H_i and I_i at all points in the octant. This problem was solved by fitting two-dimensional cubic splines to both H_i and I_i using the techniques of de Boor (1978). These subroutines are also available from IMSL. This procedure allowed rapid and accurate evaluation of H_i, I_i and their derivatives at any point within the octant.

We thank E. Abresch for his help in the preparation of the reaction center samples, H. Shore for many helpful discussions, and R. Parker for suggesting a particularly useful contour mapping technique.

This work was supported by National Science Foundation grants DMR 80-07969 and PCM 82-02811 and National Institutes of Health grant GM 13191. R. Calvo was supported by the Instituto Venezolano de Investigaciones Cientificae.

Received for publication 28 July 1983 and in final form 17 November 1983.

REFERENCES

Aasa R., and T. Vanngard. 1975. EPR signal intensity and powder shapes: a reexamination. *J. Magn. Res.* 19:308–315.

Abragam, A., and B. Bleaney. 1970. Electron paramagnetic resonance of transition metal ions. Clarendon Press. Oxford.

Allen, J. P., and G. Feher. 1984. Crystallization of reaction centers from *R. Sphaeroides* R-26. *Biophys. J.* 45(2, Pt. 2)256*a*. (Abstr.)

Bolton, J. R. 1978. Primary electron acceptors. *In* The photosynthetic bacteria. R. K. Clayton and W. R. Sistrom, editors. Plenum Publishing Corp., New York. 419–429.

Boso, B., P. G. Debrunner, M. Y. Okamura, and G. Feher. 1981*a*. Mossbauer studies of reaction centers from *R. sphaeroides*. *Biophys. J.* 33(2, Pt. 2):263*a*. (Abstr.)

Boso, B., P. G. Debrunner, M. Y. Okamura, and G. Feher. 1981*b*. Mossbauer spectroscopy studies of reaction centers from *Rhodopseudomonas sphaeroides* R-26. *Biochim. Biophys. Acta.* 638:173–177.

Brudvig, G. W., S. T. Worland, and K. Sauer. 1983. New rapid procedure for isolating photosynthetic reaction centers using cytochrome-*c* affinity chromatography. *Proc. Natl. Acad. Sci. USA.* 80:683–686.

Bunker, G., E. A. Stern, R. E. Blankenship, and W. W. Parson. 1982. An x-ray absorption study of the iron site in bacterial photosynthetic reaction centers. *Biophys. J.* 37:539–551.

Butler, W. F., D. C. Johnston, M. Y. Okamura, H. B. Shore, and G. Feher. 1978. Magnetic properties of reaction centers from *R. sphaeroides* R-26. *Biophys. J.* 21:8*a*. (Abstr.)

Butler, W. F., D. C. Johnston, H.B. Shore, D. R. Fredkin, M.Y. Okamura, and G. Feher. 1980. The electronic structure of Fe^{2+} in reaction centers from *Rhodopseudomonas sphaeroides*. I. Static magnetization measurements. *Biophys. J.* 32:967–992.

Calvo, R., W. F. Butler, R. A. Isaacson, M. Y. Okamura, D. R. Fredkin, and G. Feher. 1982. Spin-lattice relaxation time of the reduced primary quinone in RCs from *R. sphaeroides*: determination of zero-field splitting of Fe^{2+}. *Biophys. J.* 37(2, Pt. 2):111*a*. (Abstr.)

Clayton, R. K., and S. C. Straley. 1972. Photochemical electron transport in photosynthetic reaction centers. IV. Observations related to the reduced photoproducts. *Biophys. J.* 12:1221–1234.

Clayton, R. K., E. Z. Szuts, and H. Fleming. 1972. Photosynthetic electron transport in photosynthetic reaction centers from *Rhodopseudomonas sphaeroides*. III. Effects of *o*-phenanthroline and other chemicals. *Biophys. J.* 12:64–79.

Coffman, R. E., and G. R. Buettner. 1979. A limit function for long-range ferromagnetic and antiferromagnetic superexchange. *J. Phys. Chem.* 83:2387–2392.

Cogdell, R. J., D. C. Brune, and R. K. Clayton. 1974. Effects of extraction and replacement of ubiquinone upon the photochemical activity of reaction centers and chromatophores from *Rhodopseudomonas spheroides*. *FEBS (Fed. Eur Biochem Soc.) Lett.* 45:344–347.

Cotton, F. A., and G. Wilkinson. 1972. Advanced Inorganic Chemistry. John Wiley & Sons, Inc., New York. 862.

Cramer, W. A., and A. R. Crofts. 1982. Electron and proton transport. *In* Photosynthesis. Govindjee, editor. Academic Press,Inc., New York. 387–467.

Dahlquist, G., A. Bjorck, and N. Anderson. 1974. Numerical methods. Prentice-Hall, Inc., Englewood Cliffs, NJ. 233–237, 275–290.

de Boor, C. 1978. A practical guide to splines. Springer-Verlag New York. Inc., New York.

Debrunner, P. G., C. E. Schulz, G. Feher, and M. Y. Okamura. 1975. Mossbauer study of reaction centers from *R. Spheroides*. *Biophys. J.* 15(2, Pt. 2):226*a*.

Debus, R. J., M. Y. Okamura, and G. Feher. 1981. Dissociation and reconstitution of the H subunit from RCs of *R. sphaeroides* R-26. *Biophys. J.* 33(2, Pt. 2):19*a*.

Dutton, P. L., J. S. Leign, and E. W. Reed. 1973. Primary events in the photosynthetic reaction center from *Rhodopseudomonas sphaeroides* strain R-26: triplet and oxidized states of bacteriochlorophyll and the identification of the primary electron acceptor. *Biochim. Biophys. Acta.* 292:654–664.

Eisenberger, P., M. Y. Okamura, and G. Feher. 1982. The electronic structure of Fe^{2+} in reaction centers from *Rhodopseudomonas sphaeroides*. II. Extended x-ray fine structure studies. *Biophys. J.* 37:523–538.

Feher, G., and A. F. Kip. 1955. Electron spin resonance absorption in metals. I. Experimental. *Phys. Rev.* 98:337–348.

Feher, G. 1957. Sensitivity in microwave paramagnetic resonance absorption techniques. *Bell System Tech. J.* 36:449–484.

Feher, G. 1983. National Lecture, Biophysical Society Meeting. San Diego, CA.

Feher, G., R. A. Isaacson, and J.D. McElroy. 1969. Observation of EPR lines using temperature modulation. *Rev. Sci. Instrum.* 40:1640–1641.

Feher, G. 1971. Some chemical and physical properties of a bacterial reaction center particle and its primary photochemical reactants. *Photochem. Photobiol.* 14:373–388.

Feher, G., M. Y. Okamura, and J. D. McElroy. 1972. Identification of an electron acceptor in reaction centers of *Rhodopseudomonas spheroides* by EPR spectroscopy. *Biochim. Biophys. Acta.* 267:222–226.

Feher, G., A. J. Hoff, R. A. Isaacson, and J. D. McElroy. 1973. Investigation of the electronic structure of the primary electron donor in bacterial photosynthesis by the ENDOR technique. *Biophys J.* 13:61. (Abstr.)

Feher, G., R. A. Isaacson, J. D. McElroy, L. C. Ackerson, and M. Y. Okamura. 1974. On the question of the primary acceptor in bacterial photosynthesis: manganese substituting for iron in reaction centers of *Rhodopseudomonas spheroides* R-26. *Biochim. Biophys. Acta.* 368:135–139.

Feher, G., A. J. Hoff, R. A. Isaacson, and L. C. Ackerson. 1975. ENDOR experiments on chlorophyll and bacteriochlorophyll *in vitro* and in the photosynthetic unit. *Ann. NY Acad. Sci.* 244:239–259.

Feher, G., and M. Y. Okamura. 1978. Chemical composition and properties of reaction centers. *In* The photosynthetic bacteria. R. K. Clayton and W. R. Sistrom, editors. Plenum Publishing Corp., Inc., New York. 349–386.

Feher, G., and M. Y. Okamura. 1983. Proceedings of the Sixth International Congress on Photosynthesis. Brussels. In press.

Halsey, Y. D., and W. W. Parson. 1974. Identification of ubiquinone as the secondary electron-acceptor in the photosynthetic apparatus of *Chromatium vinosum*. *Biochim. Biophys. Acta.* 347:404–416.

Isaacson, R. A. 1976. Microwave coupler for EPR cavities at 1.3 K. *Rev. Sci. Instrum.* 47:973–974.

Leigh, J. S., and P. L. Dutton. 1972. The primary electron acceptor in photosynthesis. *Biochem. Biophys. Res. Comm.* 46:414–421.

Loach, P. A., and R. L. Hall. 1972. The question of the primary electron acceptor in bacterial photosynthesis. *Proc. Natl. Acad. Sci. USA.* 69:786–790.

Lynch, M. W., M. Valentine, and D. N. Hendrickson. 1982. Mixed-valence semiquinone-catecholate-iron complexes. *J. Am. Chem. Soc.* 104:6982–6989.

Martin, R. L. 1968. Metal-metal interaction in paramagnetic clusters. *In* New pathways in Inorganic Chemistry. E. A. V. Ebswoth, A. G. Maddock, and A. G. Sharpe, editors. Cambridge University Press, Cambridge. 175.

McElroy, J. D. 1970. On the nature of the light-induced free radical observed in photosynthetic bacteria. Ph.D. Thesis. University of California, San Diego. La Jolla, CA.

McElroy, J. D., G. Feher, and D. Mauzerall. 1970. Observation of a second light induced EPR signal from reaction centers of photosynthetic bacteria. *Biophys. Soc. Abstr.* 10:204*a*.

McElroy, J. D., G. Feher, and D. C. Mauzerall. 1972. Characterization of primary reactants in bacterial photosynthesis. I. Comparison of the light-induced EPR signal ($g = 2.0026$) with that of a bacteriochlorophyll radical. *Biochim. Biophys. Acta.* 267:363–374.

McElroy, J. D., D. C. Mauzerall, and G. Feher. 1974. Characterization of

primary reactants in bacterial photosynthesis. II. Kinetic studies of the light-induced EPR signal ($g = 2.0026$) and the optical absorbance changes at cryogenic temperatures. *Biochim. Biophys. Acta.* 333:261–278.

Michel, H. 1982. Three-dimensional crystals of a membrane protein complex. The photosynthetic reaction centre from *Rhodopseudomonas viridis*. *J. Mol. Biol.* 158:567–572.

Norris, J. R., M. E. Druyan, and J. J. Katz. 1973. Electron nuclear double resonance of bacteriochlorophyll free radical *in vitro* and *in vivo*. *J. Am. Chem. Soc.* 95:1680–1682.

Norris, J. R., H. Scheer, and J. J. Katz. 1975. Models for antenna and reaction center chlorophylls. *Ann. N. Y. Acad. Sci.* 244:261–280.

Norris, J. R., M. C. Thurnauer, and M. K. Bowman. 1980. Electron spin echo spectroscopy and the study of biological structure and function. *Adv. Biol. Med. Phys.* 17:365–416.

Okamura, M. Y., R. A. Isaacson, and G. Feher. 1975. Primary acceptor in bacterial photosynthesis: obligatory role of ubiquinone in photoactive reaction centers of *Rhodopseudomonas spheroides*. *Proc. Natl. Acad. Sci. USA.* 72:3491–3495.

Okamura, M. Y., R. A. Isaacson and G. Feher. 1978. EPR signals from the primary and secondary quinones in reaction centers from *R. sphaeroides* R-26. *Biophys. J.* 21:8*a*. (Abstr.)

Okamura, M. Y., G. Feher and N. Nelson. 1982. Reaction centers. *In* Photosynthesis, Energy Conversion by Plants and Bacteria. Govindjee, editor. Academic Press, Inc., New York. 195–272.

Parson, W. W., and G. D. Case. 1970. In *Chromatium*, a single photochemical reaction center oxidizes both cytochrome C_{552} and cytochrome C_{555}. *Biochim. Biophys. Acta.* 205:232–245.

Poole, C. P. 1983. Electron spin resonance. John Wiley & Sons, Inc., New York.

Portis, A. M. 1953. Electronic structure of *F* centers: saturation of the electron spin resonance. *Phys. Rev.* 91:1071–1078.

Rutherford, A. W. and M. C. W. Evans. 1980. Direct measurement of the primary and secondary quinone electron acceptors in *Rhodopseudomonas sphaeroides* (wild type) by EPR spectrometry. *FEBS (Fed. Eur. Biochem. Soc.) Lett.* 110:257–261.

Schiff, L. I. 1968. Quantum mechanics. McGraw-Hill, Inc., New York.

Slooten, L. 1972. Electron acceptors in reaction center preparations from photosynthetic bacteria. *Biochim. Biophys. Acta.* 272:208–218.

Smith, B. T., J. M. Boyle, J. J. Dongarra, B. S. Garbow, Y. Ikebe, V. C. Klema, and C. B. Moler. Matrix eigensystem routines—EISPACK guide. Springer-Verlag New York, Inc., New York.

Sogo, P., M. Jost, and M. Calvin. 1959. Evidence for free-radical production in photosynthesizing systems. *Radiat. Res. 1(Suppl.):511–518.*

Vermeglio, A. 1977. Secondary electron transfer in reaction centers of *Rhodopseudomonas sphaeroides*. Out-of-phase periodicity of two for the formation of ubisemiquinone and fully reduced quinone. *Biochim. Biophys. Acta.* 459:516–524.

Wraight, C. A. 1977. Electron acceptors of photosynthetic bacterial reaction centers. Direct observation of oscillatory behaviour suggesting two closely equivalent ubiquinones. *Biochim. Biophys. Acta.* 459:525–531.

Wraight, C. A. 1978. Iron-quinone interactions in the electron acceptor region of bacterial photosynthetic reaction centers. *FEBS (Fed. Eur. Biochem. Soc.) Lett.* 93:283–288.